HIV broadly neutralizing antibody escapability drives the therapeutic efficacy of vectored immunotherapy

Nicolas M.S. Galvez[1], Yi Cao[1], Adam D. Nitido[1], Cailin E. Deal[1], Christine L. Boutros[1], Scott W. MacDonald[1], Yentli E. Soto Albrecht[1], Evan C. Lam[1], Maegan L. Sheehan[1], Dylan Parsons[1], Allen Z. Lin[1], Martin J. Deymier[1], Jacqueline M. Brady[1], Benjamin Moon[1], Christopher B. Bullock[1], Serah Tanno[1], Amarendra Pegu[2], Xuejun Chen[2], Cuiping Liu[2], Richard A. Koup[2], John R. Mascola[2], Vladimir D. Vrbanac[1], Daniel Lingwood[1] and Alejandro B. Balazs[1*]

[1] Ragon Institute of Massachusetts General Hospital, Massachusetts Institute of Technology and Harvard University, Cambridge, MA 02139, USA

[2] Vaccine Research Center, National Institute of Allergy and Infectious Diseases and National Institutes of Health, Bethesda, MD 20892, USA

[*]Direct all correspondence to: Dr. Alejandro Balazs, Ragon Institute of MGH, MIT & Harvard, 400 Technology Square, Cambridge, MA 02139; phone: (857) 268-7000; e-mail: abalazs@mgh.harvard.edu;

Key Words: Vectored Immunotherapy, HIV, Broadly Neutralizing Antibody, Humanized Mice, AAV, Evolution, Resistance, Escapability

SUMMARY

Broadly neutralizing antibodies (bNAbs) have shown great promise for prevention and treatment of HIV infection. Breadth of bNAb neutralization, measured *in vitro* across panels of diverse viral isolates, is often used as a predictor of clinical potential. However, recent prevention studies demonstrate that the clinical efficacy of a broad and potent bNAb (VRC01) is undermined by neutralization resistance of circulating strains. Using HIV-infected humanized mice, we find that therapeutic efficacy of bNAbs delivered as Vectored ImmunoTherapy (VIT) is a function of both the fitness cost and resistance benefit of mutations that emerge during viral escape, which we term 'escapability'. Applying this mechanistic framework, we find that the sequence of the envelope V5-loop alters the resistance benefits of mutants that arise during escape, thereby impacting the therapeutic efficacy of VIT-mediated viral suppression. We also find that an emtricitabine-based antiretroviral drug regimen dramatically enhances the efficacy of VIT, by reducing the fitness of mutants along the escape path. Our findings demonstrate that bNAb escapability is a key determinant to consider in the rational design of antibody regimens with maximal efficacy and illustrates a tractable means of minimizing viral escape from existing bNAbs.

INTRODUCTION

Over the past decade, broadly neutralizing antibodies (bNAbs) capable of inhibiting infection across HIV clades have been extensively described and characterized[1,2]. Given their promise, substantial efforts have been made to develop bNAbs as HIV prevention and treatment modalities, with multiple studies demonstrating the capacity for bNAbs to prevent HIV infection in both mouse[3–8] and non-human primate (NHP) animal models[9–14]. These findings led to two harmonized phase 2b randomized controlled trials assessing the potential of the CD4bs-targeted bNAb VRC01 to prevent acquisition of HIV infection[15]. These studies found that while VRC01 prevented transmission of neutralization-sensitive strains, overall efficacy was limited by the large fraction of circulating isolates harboring resistance[16,17]. Numerous additional studies have also demonstrated the potential for bNAb administration to transiently suppress HIV viremia in multiple animal models[18–25] as well as in people living with HIV who harbor sensitive viruses[26–32]. However, these have revealed that even combinations of bNAbs can fail to control viremia as a consequence of viral escape[31,33].

BNAbs are often compared to one another using metrics obtained *in vitro* across large panels of diverse viral isolates[34]. These measurements typically consist of potency, described as the average inhibitory concentration needed to block 50% infection (IC_{50}) of all tested isolates, as well as breadth, defined as the fraction of isolates neutralized at a given antibody concentration[35]. VRC07 is an HIV envelope-specific, CD4 binding site (CD4bs) directed bNAb which exhibits greater potency and breadth *in vitro* than its clonal relative, VRC01[9,36]. VRC07 neutralizes 83% of a panel of 179 strains at less than 1 μg/mL, with a geometric mean IC_{50} of 0.11 μg/mL[9]. In prior

work, we demonstrated that VRC07, and its derivative VRC07-G54W[37], prevent acquisition of HIV during low-dose repetitive vaginal challenge in BLT humanized mice[3,8]. However, recent advances in antibody isolation have identified other promising bNAbs with median potencies as low as 0.003 μg/mL[38,39] and breadth capable of neutralizing up to 96% of a panel of 208 viruses at an IC_{50} of 1 μg/mL or less[40].

Clinical translation of these bNAbs is hindered by the need for repeated administrations to maintain effective serum concentrations due to the inevitable decay of proteins in circulation[41]. However, we and others have previously described vectored immunoprophylaxis (VIP) as a means of producing long-lived, protective concentrations of bNAbs via a single intramuscular (IM) injection[4,42–45]. VIP employs recombinant adeno-associated viral (AAV) vectors that have been engineered to deliver a bNAb-encoding human IgG transgene to tissues which produce antibodies *in vivo*[46]. Studies of VIP have demonstrated that this approach can deliver bNAbs that prevent intravenous and mucosal transmission of HIV in humanized mice[3,4,8] and SIV or SHIV in NHP models[10,47,48]. Recently, the VRC603 phase I study administered our previously validated AAV8-VRC07 vector[3] to antiretroviral therapy (ART)-suppressed patients (NCT03374202); demonstrating up-to three micrograms per milliliter of VRC07 in serum for at least three years following a single intramuscular administration[49].

In the present study, we describe the potential for Vectored ImmunoTherapy (VIT) to sustain suppression of actively replicating HIV in humanized mice. Surprisingly, we find that traditional breadth and potency metrics are poor predictors of therapeutic outcome. Instead, antibody ‘escapability’, which we define as the fitness costs and resistance benefits of mutations made along the evolutionary escape path, explains the

success or failure of VIT. Under this framework, we demonstrate that VRC07 treatment of the transmitted/founder strain $HIV_{REJO.c}$ constrains viral evolution to enforce a challenging escape path that often fails to emerge, enabling long-term suppression with a single vectored antibody. Interestingly, we find that the sequence of the V5-loop of viral envelope drives the outcome of VRC07 VIT by impacting the resistance benefits of mutations along the escape path. Lastly, we find that intentionally selecting for resistance to common antiretroviral drug regimens containing Emtricitabine exacerbates the fitness cost of mutations along the escape path; this directs the virus towards evolutionary ‘dead ends’ that enhance bNAb therapeutic efficacy to enable consistent viral suppression by VIT. Together, our data suggests that escapability represents a key determinant of bNAb therapeutic potential that can be harnessed to enhance antibody-mediated therapies against HIV.

RESULTS

VRC07 suppresses $HIV_{REJO.c}$ replication

We and others have described the use of AAV vectors to deliver an immunoglobulin-encoding transgene to muscle tissue, resulting in long-term expression and secretion of antibody into the blood[3,4,22,42–45,47,50]. To explore whether such an approach could be used as a long-lived therapeutic strategy capable of suppressing ongoing HIV replication, we employed the Bone marrow-Liver-Thymus (BLT) humanized mouse model[51]. These animals exhibit robust engraftment of human lymphocytes throughout tissues, enabling sustained infection with HIV for up to 6 months post-infection[52,53]. BLT mice were infected with $HIV_{REJO.c}$, a clade B CCR5-tropic transmitted/founder infectious molecular clone (IMC) of HIV[54], which was allowed to propagate and diversify in the host over a period of four weeks. Groups of BLT mice harboring established $HIV_{REJO.c}$ infections were given a single IM injection of AAV expressing VRC07 bNAb or a negative control of AAV expressing luciferase. Importantly, VRC07 potently neutralized the same viral stock of $HIV_{REJO.c}$ used to infect mice with an *in vitro* IC_{50} of 0.0275 µg/mL (Fig. 1a). After vector administration, VRC07 expression levels in infected mice increased over a period of six weeks, plateauing at a mean of approximately 100 µg/mL in plasma that was sustained for the remainder of the study, representing a value approximately 3,600-fold above the *in vitro* IC_{50} (Fig. 1b). Control mice given AAV-luciferase exhibited mean plasma viral loads above 10^5 copies per mL within three weeks of infection, which were largely sustained for the 26 weeks of the study (Fig. 1c). In contrast, mice given AAV-VRC07 exhibited viral loads that decreased precipitously over a three-week period, after which two divergent outcomes

were observed: viral rebound in 56% (30/54) or persistent viral control in 44% (24/54) of mice throughout the study (Fig. 1d, Extended Data Fig. 1a).

To explore whether another CD4bs-directed bNAb could achieve long-lived viral suppression, we tested N6, which represents an exceptionally broad bNAb capable of neutralizing 96% of a 181-strain global panel with an IC_{50} of less than 1 µg/mL[55]. We found that N6 had a very similar IC_{50} (0.0495 µg/mL) against the $HIV_{REJO.c}$ IMC stock as VRC07 (Fig. 1a). Humanized mice were infected with the same $HIV_{REJO.c}$ IMC stock and were given a single administration of AAV-N6 four weeks later. Plasma concentrations of N6 achieved a mean of 26 µg/mL, or nearly 525-fold higher than its *in vitro* IC_{50} against $HIV_{REJO.c}$ (Fig. 1b). However, AAV-N6 resulted in only a transient decline in viral load over the first two weeks, which returned to pre-treatment levels or higher within four weeks of vector injection in all mice (Fig. 1e); demonstrating that breadth determined via IC_{50} measured *in vitro* is not predictive of antibody efficacy *in vivo*.

We next tested a third bNAb, PGDM1400, which has been reported to be an exceptionally potent antibody that recognizes the HIV envelope trimer apex with a median IC_{50} of 0.003 µg/mL against a 77-virus panel[39], however it neutralized our $HIV_{REJO.c}$ IMC stock with an IC_{50} of 0.3697 µg/mL (Fig. 1a). We compared the efficacy of vectored PGDM1400 in BLT humanized mice infected with the same $HIV_{REJO.c}$ IMC stock as before. Following AAV administration, expression of PGDM1400 rapidly increased, reaching a mean plasma concentration of 66 µg/mL, or nearly 179-fold above its *in vitro* IC_{50} against $HIV_{REJO.c}$ (Fig. 1b). However, all mice treated with AAV-PGDM1400 displayed no significant change in viremia over the 26-week period of observation (Fig. 1f); demonstrating that potency as measured by IC_{50} *in vitro* is also not

predictive of antibody efficacy *in vivo*. Comparison of the geometric mean viral loads of $HIV_{REJO.c}$-infected BLT animals demonstrated that only those receiving AAV-VRC07 exhibited significant differences (Fig. 1g, Extended Data Fig. 1b).

To explore whether differences in the viral diversity prior to antibody treatment might explain the observed outcome, we compared the average Shannon entropy of the HIV *env* gene three weeks after infection, but prior to vector administration, and noted no significant differences between antibody treatments or luciferase controls (Extended Data Fig. 1c). Importantly, there were also no differences in diversity between AAV-VRC07 treated mice that went on to rebound or be suppressed. When comparing rebounding AAV-VRC07 treated mice to suppressed mice, we found that mice in each group had indistinguishable levels of VRC07 antibody (Extended Data Fig. 1d), but had a small but statistically significant difference in viral load at the time of AAV administration (Fig. 1h).

Together, these studies demonstrate that only AAV-VRC07 could suppress actively replicating $HIV_{REJO.c}$. In contrast, treatment with other potent bNAbs had negligible effects on the viral load of infected BLT mice despite comparable viral diversity and bNAb potency (Fig. 1i).

VRC07 fails to control HIV_{JR-CSF}

Given the ability of VRC07 to reproducibly suppress $HIV_{REJO.c}$ infection in a subset of mice, we sought to determine whether it could also suppress other HIV isolates. HIV_{JR-CSF} is a Clade B CCR5-tropic primary isolate originally obtained from the cerebrospinal fluid of a chronically HIV^+ subject[56]. We generated HIV_{JR-CSF} viral stock

from an IMC plasmid which was neutralized *in vitro* by VRC07 with an IC_{50} of 0.0836 µg/mL (Extended Data Fig. 2a). Groups of humanized mice were infected with $HIV_{JR\text{-}CSF}$ prior to receiving AAV expressing either luciferase or VRC07. Antibody expression was similar to mice in previous experiments, achieving geometric mean plasma concentrations above 300 µg/mL, which is more than 4000-fold above the *in vitro* IC_{50} (Extended Data Fig. 2b). In contrast to the previous study with $HIV_{REJO.c}$, $HIV_{JR\text{-}CSF}$-infected mice exhibited no change in viral load following AAV-VRC07 administration and were indistinguishable from the AAV-luciferase controls (Extended Data Fig. 2c, 2d).

To determine whether other bNAbs might be effective in suppressing $HIV_{JR\text{-}CSF}$, we tested AAV-N6 and AAV-PGDM1400 as described above. Both of these antibodies potently neutralized $HIV_{JR\text{-}CSF}$ viral stock *in vitro*, with IC_{50} values of 0.2715 and 0.0973 µg/mL, for N6 and PGDM1400 respectively (Extended Data Fig. 2a). Following administration of AAV encoding each bNAb, mean plasma antibody titers plateaued four weeks post-administration at 4.2 µg/mL for N6 and 15.4 µg/mL for PGDM1400 (Extended Data Fig. 2b). Despite expression of N6 and PGDM1400 at levels ranging from 15 to 158-fold above their IC_{50}, we observed no impact on viral load (Extended Data Fig. 2e,f), demonstrating that none of the AAV-bNAbs tested was capable of suppressing established $HIV_{JR\text{-}CSF}$ infections at the levels of antibody achieved (Fig. 1j).

Antibody escapability is defined by the costs and benefits of resistance mutations

To understand the basis for differences in VRC07 effectiveness against $HIV_{REJO.c}$, as compared to $HIV_{JR\text{-}CSF}$, we dissected the evolutionary escape path selected by each antibody-strain pair. Plasma viral RNA obtained at the conclusion of

the prior studies was deep sequenced to explore the mutations arising during viral escape. Individual HIV-infected mice receiving AAV-luciferase exhibited mutations distributed throughout the $HIV_{REJO.c}$ and HIV_{JR-CSF} envelopes (Extended Data Fig. 3a-b, top). Interestingly, in the absence of bNAb selection pressure, these mutations formed no discernable pattern in HIV_{REJO} envelope sequences (Extended Data Fig. 3c), but HIV_{JR-CSF} exhibited consistent mutations just outside the V3 loop (Extended Data Fig. 3d), which translated into loss of a glycosylation site at position N339 not observed for $HIV_{REJO.c}$ (Extended Data Fig. 3e,f).

In contrast, nearly all sequences obtained from $HIV_{REJO.c}$-infected animals that escaped from VRC07 exhibited two possible pairs of mutations: either two D-loop mutations (N276D and D279A) or, more commonly, a D-loop and a V5-loop mutation (D279A and N460D, respectively) (Extended Data Fig. 3a, bottom). When assessed collectively across all escaped mice, these three mutations represented the majority of amino acid divergence from the parental sequence (Fig. 2a). The N460D mutation also resulted in a sequon loss in the V5-loop of $HIV_{REJO.c}$ (Extended Data Fig. 3g). In contrast, AAV-VRC07 treatment of HIV_{JR-CSF}-infected mice selected primarily for a single D-loop mutation at position D279 (Fig. 2b, Extended Data Fig. 3b, bottom) with a minority of mice exhibiting loss of a sequon at N276 (Extended Data Fig. 3h).

To determine the impact of these mutations on bNAb resistance and viral fitness, each individual mutation and combination observed in haplotypes were engineered into $HIV_{REJO.c}$ or HIV_{JR-CSF} IMC plasmids to produce replication-competent mutant viruses. Each mutant virus was first tested for neutralization sensitivity against VRC07 *in vitro* (Fig. 2c, d). When assessed individually, neither N276D nor N460D demonstrated any

resistance to VRC07 neutralization of $HIV_{REJO.c}$, but D279A led to partial escape by mediating a 51-fold increase in the IC_{50} to 1.4 µg/mL (Supplementary Table 1). However, complete escape from high concentrations of VRC07 (>200 µg/mL) was only observed for envelopes containing both D279A and either N460D or N276D (Fig. 2c). In contrast, HIV_{JR-CSF} mutants encoding a single D279A or D279H mutation within the D-loop resulted in complete escape from high concentrations of VRC07 (>200 µg/mL) (Fig. 2d).

To measure the fitness cost of $HIV_{REJO.c}$ and HIV_{JR-CSF} VRC07 escape mutations, we determined the growth rate of each envelope mutant using qPCR-based quantitation of genome copies over time for infected primary $CD4^+$ T cells across large numbers of replicate infections (n=16), which were then fit to a growth model (Fig. 2e,f) [57]. Interestingly, we observed that $HIV_{REJO.c}$ mutation D279A alone, which conferred partial escape from VRC07, grew 2.3-fold slower than the parental strain (Fig. 2e). Moreover, one of the additional mutations needed to achieve complete neutralization resistance (N460D) was associated with further loss of fitness. In the case of HIV_{JR-CSF}, D279A and D279H were also found to grow more slowly than the parental strain, suggesting a modest loss of fitness for these mutants (Fig. 2f).

To represent the relationship between fitness cost and escape benefit visually, we generated escapability maps representing potential pathways of escape *in vivo*. During $HIV_{REJO.c}$ escape from VRC07, we observed three potential mutations that were one amino acid change away from parental virus. However, only D279A achieved modest neutralization resistance, which was coupled to decreased fitness. Further resistance required a second mutation to achieve complete escape, with one reducing

(N276D), and another increasing (N460D), fitness cost (Fig. 2g, top). In contrast, complete escape of $HIV_{JR\text{-}CSF}$ from VRC07 could occur through at least two different single amino acid changes from the parent strain with modest fitness costs (Fig 2g, bottom).

We similarly analyzed both $HIV_{REJO.c}$ and $HIV_{JR\text{-}CSF}$ mutants selected by AAV-N6 (Extended Data Fig. 4) to produce their respective escapability maps. We found that AAV-N6 typically selected for a single nucleotide change to yield a A281D mutation in sequencing reads from $HIV_{REJO.c}$-infected mice, leading to significant escape from N6 at high fitness cost. Interestingly, a minority of sequencing reads contained two nucleotide mutations, resulting in an A281K variant which completely escaped N6 with lower fitness cost (Fig 2h, top). By comparison, in animals infected with $HIV_{JR\text{-}CSF}$, N6 selected for either a single A281D mutation, which granted moderate resistance at high fitness cost, or the combination of A281D with N276D to yield complete escape at lower fitness cost (Fig. 2h, bottom).

Finally, we analyzed both $HIV_{REJO.c}$ and $HIV_{JR\text{-}CSF}$ mutants selected by AAV-PGDM1400 (Extended Data Fig. 5) to produce their respective escapability maps. Across both strains, we observed significant divergence centered around the V1/V2 loop near the well-characterized glycosylation site at position N160. Interestingly, the escapability plots for both strains suggested multiple routes of escape, each of which result in loss of the glycan site at position N160 and which had no significant fitness cost (Fig. 2i).

Taken together, these results suggest that the unique ability of VRC07 alone to control $HIV_{REJO.c}$ is a consequence of the relatively high fitness cost and partial

resistance granted by the initial D279A mutation, with multiple steps needed to achieve complete neutralization resistance, which was not observed for other antibodies.

Escapability is influenced by envelope sequence context

Our experiments demonstrate that $HIV_{REJO.c}$ and HIV_{JR-CSF} exhibit differences in escape paths under VRC07 selection. However, these studies could not discern whether differences in envelope sequence or inherent fitness differences between strains contributed to escapability. To dissect the contribution of sequence context on bNAb escape, we engineered chimeric infectious molecular clones of $HIV_{REJO.c}$ and HIV_{JR-CSF} that contained swaps of amino acid sequences comprising the D-loop, the V5-loop or both loops between these two strains (Fig. 3a). Each of the resulting six chimeric and two parental strains were efficiently neutralized by VRC07, with IC_{50} measurements falling between 0.024 and 0.190 µg/mL (Extended Data Fig. 6a). Importantly, both $HIV_{REJO.c}$ and HIV_{JR-CSF} that were chimeric for the V5-loop alone exhibited fitness very similar to the parent strains, whereas $HIV_{REJO.c}$ chimeras that swapped the D-loop exhibited slower growth (Extended Data Fig. 6b). Following infection of BLT humanized mice with each chimeric strain, AAV-VRC07 was administered, resulting in geometric mean steady-state plasma antibody concentrations of approximately 100µg/mL (Extended Data Fig. 6c). As expected, given our prior results, AAV-VRC07 administration resulted in a subset of $HIV_{REJO.c}$-infected mice exhibiting viral suppression, while all HIV_{JR-CSF}-infected mice escaped (Fig. 3b, Extended Data Fig. 6d). A similar proportion of mice infected with $HIV_{REJO.c}$ containing the JR-CSF D-loop (HIV_{RD}) were suppressed by VRC07, while mice infected with HIV_{JR-CSF} containing

REJO.c D-loop (HIV_{JD}) all escaped. In contrast, all mice infected with $HIV_{REJO.c}$ containing JR-CSF V5-loop (HIV_{RV}) exhibited rapid escape from VRC07, while a subset of mice infected with HIV_{JR-CSF} containing the REJO.c V5-loop (HIV_{JV}) were transiently suppressed. Finally, mice infected with $HIV_{REJO.c}$ containing both the D loop and V5 loop from JR-CSF (HIV_{RDV}) resulted in an intermediate suppression phenotype between RD and RV after VRC07 treatment. However, mice infected with HIV_{JR-CSF} containing both the D loop and V5 loop from REJO.c (HIV_{JDV}) resulted in complete escape (Fig. 3b, Extended Data Fig. 6d).

Given the outcome of these studies, we focused on viruses that were chimeric in the V5-loop to understand why these swaps resulted in different suppression outcomes than parental strains. In contrast to $HIV_{REJO.c}$, mutations arising in HIV_{RV}-infected animals receiving AAV-VRC07 were confined to the D-loop, while those arising in HIV_{JV}-infected animals harbored mutations in both D and V5-loops, which was opposite to the pattern observed for the parental strains (Fig. 3c, Extended Data Fig. 7a-d). HIV_{RV} harboring a single amino acid change at D279 was sufficient to completely escape from VRC07, at substantial fitness cost (Fig. 3d, Extended Data Fig. 7e,f, left). By comparison, only partial escape from VRC07 occurred following D279A mutation in HIV_{JV}, with complete escape requiring two mutations but with limited fitness cost (Fig. 3d, Extended Data Fig. 7e,f, right). These data suggest that the sequence context of the HIV envelope directly influences the path taken to escape from VRC07.

Escape is fitness-dependent

Given the importance of sequence context in defining the relative benefit of mutations along the evolutionary escape path, we sought to define the impact of viral fitness on escape potential. To explore this axis of escapability, we looked for a means of altering the fitness of the virus independent of envelope sequence to determine its impact on escape. Given the previously described reduction in viral fitness following escape from emtricitabine-based drug regimens[58], we aimed to intentionally drive the emergence of polymerase gene (pol) mutations through sub-optimal dosing of antiretroviral therapy (ART) in humanized mice.

To achieve this, we infected BLT mice with $HIV_{REJO.c}$ and provided them with a low, but escalating, dose of antiretroviral drug in their feed, starting at 0.01 times a standard human equivalent dose at week 2, increasing to 0.1 times by week 3, and reaching a full dose by week 6. At week 8 after HIV infection, either AAV-VRC07 or AAV-luciferase was administered. Two weeks after AAV administration, antiretroviral drug treatment was withdrawn (Fig. 4a). Importantly, at the time of AAV administration, no meaningful differences in viral loads were seen between the mice that had received escalating antiretroviral drugs relative to control mice (Extended Data Fig. 8a). As intended, HIV *pol* sequences isolated from mice receiving the suboptimal ART dosing displayed a near-complete prevalence of M184V/I in the polymerase gene at the time of VRC07 administration. Of note, M184V/I are mutations previously identified in humans during escape from antiretroviral treatment[58] (Fig. 4b). Antiretroviral drug treatment had no impact on the AAV-driven expression of VRC07, with treated mice achieving a geometric mean steady-state plasma antibody concentration of 79 µg/mL (Fig. 4c). ART-treated mice receiving the AAV-luciferase negative control maintained steady viral

loads, with minor but noticeable dips at each escalation of drug concentration (Fig. 4d). Administration of AAV-VRC07 without antiretroviral treatment resulted in only partial suppression of HIV, as observed in our prior experiments (Extended Data Fig. 8b). However, ART-escaped mice infected with $HIV_{REJO.c}$ that harbored M184V/I Pol mutations were completely suppressed following AAV-VRC07 (Fig. 4e,f).

Engineering polymerase mutations M184V or M184I into the original IMC vector resulted in no discernible changes in neutralization sensitivity to VRC07 or viral fitness (Extended Data Fig. 8c,d). However, when polymerase mutations were evaluated in the context of previously observed $HIV_{REJO.c}$ envelope mutations (i.e., N276D, D279A, N460D, and their combinations) there was a significant increase in fitness cost, with no evident changes in neutralization sensitivity (Extended Data Fig. 8e,f). The net effect of this was a shift in the escapability map for $HIV_{REJO.c}$ with M184V polymerase, such that complete escape through a second envelope mutation incurred substantially higher fitness costs than in $HIV_{REJO.c}$ with WT polymerase (Fig. 4g). Taken together, these results suggest that ART-escape leading to the emergence of M184 polymerase mutations makes escape from VRC07 significantly more difficult.

DISCUSSION

Antibody immunotherapy for the treatment or prevention of HIV infection is currently being trialed in numerous studies. While bNAb combinations have shown promise[59–61], individual bNAbs have demonstrated limited activity in the context of viremic patients due to antibody half-life or escape[27,28,30,32,62,63]. Here we demonstrate that vectored delivery of a single bNAb, well-matched to the infecting strain, is capable of continuously suppressing a subset of viremic humanized mice. Importantly, this efficacy was not correlated with antibody neutralization potency determined *in vitro* against the infecting viral stock or breadth metrics derived from global pseudovirus panels. Rather, our results demonstrate that the viral escape trajectory, or escapability, is the relevant parameter predicting bNAb efficacy *in vivo*.

Importantly, this was not purely a function of the binding site, given that N6 also targets the CD4bs but did not achieve viral suppression in our *in vivo* experiments. Despite its outstanding potency and breadth against diverse pseudovirus panels, we found that a single base pair change in the D-loop of $HIV_{REJO.c}$ or $HIV_{JR\text{-}CSF}$ yielded resistance to N6 neutralization above the steady-state concentrations achieved in our experiments. While higher steady-state levels of N6 might have resulted in viral suppression, we found expression of this particular antibody to be difficult, in agreement with previous reports using other delivery modalities[64].

Similarly, treatment with a V1/V2-targeting bNAb (PGDM1400) selected for numerous single base pair mutations that yielded complete escape by both $HIV_{REJO.c}$ and $HIV_{JR\text{-}CSF}$ with minimal impact on fitness. Given that numerous single base-pair changes can disrupt an NxS/T glycosylation sequon, and the limited fitness cost of

associated glycan changes, it is likely that glycan-deficient variants will be present at high frequency in a viral population. This notion is supported by the observation that a majority of viral rebound in patients treated with 10-1074, a V3-loop-targeting bNAb, was due to loss of the N332 glycan, suggesting glycan-based escape can also occur in humans[28]. Phylogenetic analysis of virus rebounding in these patients showed that 10-1074 escape variants arose from multiple distinct viral lineages, analogous to the diverse escape mutations observed in our humanized mouse studies.

In contrast to escape from PGDM1400 and N6, complete $HIV_{REJO.c}$ escape from VRC07 involved multiple mutations. These included an initial D-loop mutation at D279A, resulting in partial resistance with moderate fitness cost, and a second mutation in either the D- or V5-loops which conferred complete resistance. It should be noted that despite requiring two steps, $HIV_{REJO.c}$ escape from VRC07 occurred numerous times in our studies, suggesting that even difficult paths are viable, albeit with lower frequency. Of note, D279A was previously identified in the virus of the donor from whom VRC07 and VRC01 bNAbs were originally isolated, but was accompanied by additional mutations to restore viral fitness[29]. Our studies with chimeric viruses demonstrate the crucial role of sequence context in determining the resistance benefit of a given mutation, thereby influencing antibody escapability.

Furthermore our results demonstrate that we can actively constrain the trajectory of viral escape through drug intervention. Given the inherent pressure for low-fitness variants to revert to wildtype sequences, we employed an escalating dose of emtricitabine-containing ART to drive the selection of resistance mutations in Pol, which have been previously shown to reduce replication capacity[58]. When vectored VRC07

was administered to $HIV_{REJO.c}$-infected animals harboring these polymerase mutations, the therapeutic efficacy of VRC07 was dramatically enhanced, enabling consistent viral suppression of all animals in this experiment. When evaluating the impact of these polymerase mutations in the context of envelope sequence mutants, we found that viruses harboring M184V polymerase grew more slowly than the parental strain, suggesting that the improved efficacy of vectored VRC07 in these experiments was the result of a more challenging escape path. Whether analogous improvements in the clinical efficacy of bNAbs could be achieved by reducing the fitness of viruses replicating in patients who have failed ART regimens remains to be determined.

Overall, our results are in agreement with prior studies showing that altering the CD4bs is more likely to impact viral fitness, due to the necessity for CD4-binding during viral infection, as compared to variable loop mutations[29,65]. Consistent with this, 3 out of 8 patients treated with a 3BNC117, a CD4bs-directed bNAb, remained sensitive following viral rebound after treatment[27]. Additionally, patients undergoing ART treatment interruption following 3BNC117 administration remained suppressed until antibody levels sufficiently declined, suggesting a lack of pre-existing escape variants in the latent viral reservoir[66]. Recent characterization of escape from eCD4-Ig, a potent CD4-based fusion protein containing a small CCR5-mimetic sulfopeptide, further highlights the difficulty of viral escape from CD4bs-targeted therapeutics[65]. This again is in line with our experiments, as increasing fitness costs led to almost complete suppression *in vivo*, despite no significant changes for the IC_{50} values of any mutations along the escape path. Collectively, these findings point to the importance of escapability in achieving viral suppression and highlight the advantage of targeting high

fitness-cost epitopes. Whether similar outcomes might be obtained through vectored delivery of a single bNAb in infected humans remains unknown.

Given our findings, identifying antibodies with particularly low escapability across a broad array of strains may be more important than selecting antibodies solely on the basis of breadth and potency. These metrics are typically measured against a single round of pseudovirus infection, thus describing activity against a homogeneous target. In contrast, antibody-mediated suppression of replicating HIV faces a diverse and constantly evolving population that is shaped by selective pressure. The BLT mouse model enables systematic comparison of the therapeutic efficacy of individual bNAbs and identification of escape pathways taken by authentic HIV strains. However, their deficits in humoral and innate immunity leaves these animals largely dependent upon the delivered bNAb to exert envelope-specific selective pressure. In this context, it is possible that bNAb-based suppression of viremic humanized mice represents a relatively high bar. Viremic patients receiving individual bNAbs have exhibited more substantial drops in viral load than was seen in our models[27,28,33,62]. Additionally, there have been reports of synergy between passively transferred bNAbs and endogenous antibody responses in patients[67], which would be unlikely to occur in humanized mice. Despite these caveats, our studies enable systematic comparison of bNAb therapeutic efficacy between antibody clones in groups of genetically identical animals harboring equivalent viral infections without the confounding variables of host genetics or endogenous antibody responses.

In summary, potency and breadth metrics measured using global panels do not predict the therapeutic efficacy of bNAbs in a humanized mouse model of HIV infection.

Instead, we demonstrate that the viral escape trajectory induced by a bNAb explains the potential to suppress viremia. New methods capable of elucidating escape in tissue culture have been developed[68,69], however these are currently unable to recapitulate the magnitude of envelope diversity and selection pressure of growth *in vivo.* Given the endogenous immune responses that arise in infected non-human primates, humanized mice represent an ideal model for experimentally 'pre-screening' bNAb escape on authentic HIV strains *in vivo.* Quantification of the escapability of existing and future bNAbs will be critical for the rational design of bNAb combinations that maximize selective pressure to maintain viral suppression and prevent escape in patients.

LIMITATIONS OF THE STUDY:

Differences in bNAb neutralization potency against the strains tested in this study may influence the evolution of escape mutations. While bNAb expression *in vivo* was significantly above IC_{50} values, each vectored bNAb achieved different steady-state levels in our experiments which could have resulted in differences in selection pressure. In addition, vectored antibody delivery is slower than passive transfer of purified bNAb protein, which could have resulted in more rapid selection pressure and different outcomes. Although humanized mice enable the study of HIV replication and escape with strains obtained from patients, their relatively small blood volume, and lack of secondary lymphoid organs, may not reflect the same structure of viral populations observed in patients. In addition, this animal model does not elicit strong humoral immunity capable of neutralizing the virus, thereby lacking this important additional selection pressure that would be present in humans. Our studies only tested two

subtype B infectious molecular clones of HIV which were allowed to diversify over a four-week period, which may not reflect outcomes with more diverse isolates found in patients. Moreover, our study focuses on escape mutations present at the conclusion of the experiment, thereby missing dynamic events occurring over the course of escape. Measurements of viral growth rates were performed *in vitro* with PBMCs from a single donor, which may not reflect the fitness of these mutants across genetically distinct patients.

ACKNOWLEDGEMENTS

We wish to thank Dennis Burton (Scripps) for providing antibody proteins, Dan Barouch for providing anti-PGDM1400 idiotype antibody protein. We also thank K. L. Clayton and D. T. Claiborne for advice on experimental design and the manuscript. C.E.D. was supported by Ruth L. Kirschstein National Research Service Award (NRSA) Individual Postdoctoral Fellowship 1F32AI125096-01A1, J.M.B. was supported by Ruth L. Kirschstein Predoctoral Individual National Research Service Award 1F31AI131747-01A1, A.B.B. was supported by the National Institute for Allergy and Infectious Disease Career Transition Award K22AI102769, Research Grants R01AI174875, R01AI174276, the National Institutes for Drug Abuse (NIDA) Avenir New Innovator Award DP2DA040254, the MGH Transformative Scholars Program as well as funding from the Charles H. Hood Foundation. This independent research was supported by the Gilead Sciences Research Scholars Program in HIV.

AUTHOR CONTRIBUTIONS

C.E.D. and A.B.B. designed the experiments. N.M.S.G., Y.C., C.E.D., C.L.B., S.W.M., Y.E.S.A., E.C.L., A.L., D.P., A.D.N., M.J.D., B.M., and C.B.B. carried out experiments and analyzed data. J.M.B., A.P., X.C., R.A.K., J.R.M. and D.L. offered suggestions for experiments and provided key materials. S.T. and V.D.V. provided humanized mice. N.M.S.G., A.D.N, Y.C., C.E.D. and A.B.B. wrote the paper with contributions from all authors.

DECLARATION OF INTERESTS

A.B.B. is a founder of Cure Systems LLC.

FIGURE LEGENDS

Figure 1: Vectored delivery of VRC07, but not PGDM1400 or N6, can suppress established $HIV_{REJO.c}$ infection.

a, *In vitro* neutralization of $HIV_{REJO.c}$ by VRC07, N6, or PGDM1400 bNAbs. Data are plotted as mean ± s.e.m.

b, ELISA-based quantitation of gp120-binding antibodies in the serum of $HIV_{REJO.c}$-infected humanized mice following administration of $5x10^{11}$ genome copies (GC) of AAV-luciferase, AAV-VRC07, AAV-N6, or AAV-PGDM1400 vectors. Black arrow denotes vector administration. Data are plotted as geometric mean ± geometric SD.

c-f, HIV viral load in plasma of $HIV_{REJO.c}$-infected mice treated with AAV-luciferase control (**c**), AAV-VRC07 (**d**), AAV-N6 (**e**), or AAV-PGDM1400 (**f**). Black arrows denote vector administration. Each colored line depicts an individual mouse. The qPCR lower limit of detection was 1,000 copies mL-1 (solid line). Data are presented as mean ± s.e.m.

g, Geometric mean viral load of mice in **c-f** following vector administration over the period of observation. (p=0.0003 (One-way ANOVA with Dunnet's post-hoc test)). Error bars indicate the geometric SD.

h, HIV viral load in plasma of $HIV_{REJO.c}$-infected mice that exhibited escape or became suppressed following AAV-VRC07 vector administration (p=0.0448 (unpaired two-tailed Student's t-test)). Data are geometric mean ± geometric SD.

i, j, Kaplan-Meier plot of viral suppression in BLT humanized mice infected with either $HIV_{REJO.c}$ (**i**) or HIV_{JR-CSF} (**j**) given the indicated bNAb-expressing vector (ns: non-significant (Mantel-Cox Log-rank test comparing against the Luciferase control)). For the purposes of clarity, % HIV suppressed is defined as the fraction of mice that had not yet escaped as described in the methods.

Figure 2: Escape mutations result in distinct fitness costs and resistance benefits for $HIV_{REJO.c}$ and HIV_{JR-CSF}.

a,b, Amino acid divergence from the reference strain for $HIV_{REJO.c}$ (**a**) or HIV_{JR-CSF} (**b**) across all animals following AAV-VRC07 treatment as determined by Illumina Deep Sequencing of envelope from plasma viral RNA isolated from the final experimental timepoint. The X-axis represents the envelope protein amino acid position relative to HXB2 numbering. The Y-axis represents the average amino acid divergence from the parent strain, corrected for divergence observed in control mice.

c,d, *In vitro* neutralization assay of $HIV_{REJO.c}$ (**c**) or HIV_{JR-CSF} (**d**) harboring divergent amino acids identified in **a** and **b**, against serial dilutions of VRC07. Data are plotted as mean ± s.e.m.

e,f, *In silico* viral growth curves of $HIV_{REJO.c}$ (**e**) or HIV_{JR-CSF} (**f**) harboring divergent amino acids identified in a and b, in activated PBMC's generated using growth rates derived from QuickFit assays. Data are plotted as mean ± 95% C.I.

g-i, Escapability maps denoting fitness cost (relative doubling time) and resistance benefits (neutralization resistance) for each $HIV_{REJO.c}$ (**top**) or HIV_{JR-CSF} (**bottom**) mutant observed during escape from VRC07 (**g**), N6 (**h**), or PGDM1400 (**i**). Dashed vertical line denotes geometric mean antibody serum concentrations after vectored bNAb administration. Shaded areas represent the limits of detection. Solid arrows

represent the likely path taken with dashed arrows representing alternative paths to escape.

Figure 3: V5-loop sequences dictate escape outcomes for chimeric $HIV_{REJO.c}$ and HIV_{JR-CSF} viruses.

a, Diagram depicting $HIV_{REJO.c}$ and HIV_{JR-CSF} D-loop and V5-loop sequences present in each chimeric virus.

b, Kaplan-Meier plot of viral suppression in humanized mice infected with either $HIV_{REJO.c}$ (**left**) or HIV_{JR-CSF} (**right**) harboring chimeric D and V5-loops following vectored VRC07 administration (ns: non-significant (Mantel-Cox Log-rank test comparing against the WT strain)). For the purposes of clarity, % HIV suppressed is defined as the fraction of mice that had not yet escaped as described in the methods.

c, Amino acid divergence from the parental strain for $HIV_{REJO.c}$ (**a**) or HIV_{JR-CSF} (**b**) harboring a chimeric V5-loop across all animals following AAV-VRC07 treatment as determined by Illumina Deep Sequencing of envelope from plasma viral RNA isolated from the final experimental timepoint. The X-axis represents the envelope protein amino acid position relative to HXB2 numbering. The Y-axis represents the average amino acid divergence from the parent strain, corrected for divergence observed in control mice.

d, Escapability maps denoting fitness cost (relative doubling time) and resistance benefits (neutralization resistance) of mutations observed in $HIV_{REJO.c}$ (**left**) or HIV_{JR-CSF} (**right**) harboring a chimeric V5-loop during escape from VRC07. Dashed vertical line denotes geometric mean bNAb concentrations after vectored VRC07 administration. Shaded areas represent the limits of detection. Solid arrows represent the likely path taken with dashed arrows representing alternative paths to escape.

Fig 4: ART escape results in decreased viral fitness which enhances the therapeutic efficacy of vectored VRC07.

a, Diagram depicting the experimental timeline of sub-optimal ART treatment of $HIV_{REJO.c}$-infected humanized mice.

b, Percentage of M184V/I mutation observed in HIV polymerase at week 8, just prior to AAV-VRC07 administration. Data are presented as mean ± s.e.m.

c, ELISA-based quantitation of gp120-binding human IgG antibodies in serum of $HIV_{REJO.c}$-infected humanized mice following injection of $5x10^{11}$ GC of AAV-luciferase or VRC07. Black arrow denotes vector administration. Data are plotted as geometric mean ± geometric SD.

d,e, $HIV_{REJO.c}$ viral load in plasma during escape from ART drugs and following administration of (**e**) AAV-luciferase or (**f**) AAV-VRC07. Black arrows denote vector administration. Each colored line depicts an individual mouse and gray shading depicts the average luciferase viral load (n=4). The limit of detection was 1,000 copies per mL. Data are presented as mean ± s.e.m.

f, Kaplan-Meier plot of viral suppression in BLT humanized mice infected with $HIV_{REJO.c}$ treated or not with ART, given the VRC07 vector (ns: non-significant (Mantel-Cox Log-rank test comparing against the ART + Luciferase control)). For the purposes of clarity, % HIV suppressed is defined as the fraction of mice that had not yet escaped as described in the methods.

g, Escapability maps denoting fitness cost (relative doubling time) and resistance benefits (neutralization resistance) for each $HIV_{REJO.c}$ mutant observed during escape from VRC07. Shaded areas represent the limits of detection. Solid arrows represent the likely path taken with dashed arrows representing alternative paths to escape. Darker symbols (diamonds) and text represent envelope mutations on an M184V polymerase mutant background while lighter symbols (circles) and text represent the previously presented data for envelope mutations on a WT polymerase background.

EXTENDED DATA FIGURE LEGENDS

Extended Data Fig. 1: AAV-VRC07 can suppress $HIV_{REJO.c}$-infected BLT humanized mice.

a, HIV viral load in plasma of $HIV_{REJO.c}$-infected mice treated with AAV-VRC07. Each colored line depicts an individual mouse. The qPCR lower limit of detection was 1,000 copies mL^{-1} (solid line). Data are presented as mean ± s.e.m. Individual AAV-VRC07 treated mice that went on to escape or be suppressed are denoted by light or dark red colors, respectively.

b, Geometric mean viral load of mice in **a** following vector administration over the period of observation. (***:$p<0.005$; ****:$p<0.001$; ns:non-significant (One-way ANOVA with *Dunnet's* post-hoc test)). Error bars indicate geometric SD.

c, HIV diversity prior to vector administration as quantified by average Shannon entropy of envelope-amplicons measured by deep sequencing (ns=non-significant (One-way ANOVA with *Dunnet's* post-hoc test, comparing every group against the Luciferase control)). Data are presented as mean ± s.e.m.

d, Geometric mean of VRC07 antibody concentration in plasma following AAV-VRC07 vector administration in mice that exhibited escaped or suppressed $HIV_{REJO.c}$ (ns:non-significant ($p=0.1305$) (Unpaired two-tailed Student's t test)). Error bars indicate geometric SD.

Extended Data Fig. 2: Vectored delivery of VRC07, N6, or PGDM1400 bNAbs fails to suppress HIV_{JR-CSF}-infected BLT humanized mice.

a, *In vitro* neutralization of HIV_{JR-CSF} by VRC07, PGDM1400, or N6. Data are plotted as mean ± s.e.m.

b, ELISA-based quantitation of bNAbs in serum of HIV_{JR-CSF}-infected humanized mice following injection of between $1\text{-}5\times10^{11}$ GC of AAV-VRC07, AAV-PGDM1400, or AAV-N6. AAV-2A10 or AAV-luciferase vectors were used as negative controls. Black arrow denotes vector administration. Data are plotted as geometric mean ± geometric SD.

c-f, HIV viral load in plasma of HIV_{JR-CSF}-infected BLT mice following administration of AAV-luciferase or AAV-2A10 controls (**c**), AAV-VRC07 (**d**), AAV-N6 (**e**), or AAV-PGDM1400 (**f**). Black arrows denote vector administration. Each colored line depicts an individual mouse. The qPCR lower limit of detection was 1,000 copies mL^{-1} (solid line). Data are presented as mean ± s.e.m.

Extended Data Fig. 3: Consistent haplotypes are observed across multiple HIV-infected mice.

a,b, Haplotypes of individual mice infected with $HIV_{REJO.c}$ (**a**) or HIV_{JR-CSF} (**b**) treated with vectored VRC07 as revealed by deep sequencing of envelope genes from plasma viral RNA obtained at the final experimental timepoint. Each row represents the consensus sequence from a single mouse. Both control (top) and VRC07 (bottom) treated mice are shown. Numbers to the right of the bottom box represent the geometric mean expression of VRC07 (µg/mL) in each animal throughout the experiment. The X-axis represents the envelope amino acid position relative to HXB2 numbering. Yellow shading denotes position of individual loops within the HIV envelope (as indicated at the top).
c,d, Amino acid divergence from the reference strain for $HIV_{REJO.c}$ (**c**) or HIV_{JR-CSF} (**d**) across all control animals as determined by Illumina Deep Sequencing of envelope from plasma viral RNA isolated from the final experimental timepoint. The X-axis represents the envelope protein amino acid position relative to HXB2 numbering. The Y-axis represents the average amino acid divergence from the parent strain.
e-h, Glycosylation site divergence in control-treated (**e**,**f**) or VRC07-treated (**g**,**h**) mice as compared to the parental strain for $HIV_{REJO.c}$ (**e**,**g**) or HIV_{JR-CSF} (**f**,**h**) as determined by Illumina Deep Sequencing from plasma viral RNA isolated from the final experimental timepoint. The X-axis represents the envelope protein amino acid position of each potential N-linked glycosylation relative to HXB2 numbering. The Y-axis represents the average divergence from the parental strain envelope glycosylation sites. Plots g and h are corrected for glycan divergence seen in control mice. Potential N-linked glycosylation sites in the sequences were defined as Asn-X-Thr/Ser (NXT/S, with X being any amino acid but Pro) and the reference sequences with their respective haplotype frequencies are shown at the top of each table.

Extended Data Fig. 4: Vectored delivery of N6 selects for individual D-loop mutations that mediate resistance.
a, b, Haplotypes of individual mice infected with $HIV_{REJO.c}$ (**a**) or HIV_{JR-CSF} (**b**) treated with vectored N6 as revealed by deep sequencing of envelope genes from plasma viral RNA obtained at the final experimental timepoint. Each row represents the consensus sequence from a single mouse. Both control (**top**) and N6 (**bottom**) treated mice are shown. Numbers to the right of the bottom box represent the geometric mean expression of N6 (µg/mL) in each animal throughout the experiment. The X-axis represents the envelope amino acid position relative to HXB2 numbering. Yellow shading denotes position of individual loops within the HIV envelope (as indicated at the top).
c,d, Amino acid divergence from the reference strain for $HIV_{REJO.c}$ (**c**) or HIV_{JR-CSF} (**d**) across all N6-treated animals as determined by Illumina Deep Sequencing of envelope from plasma viral RNA isolated from the final experimental time point. The X-axis represents the envelope protein amino acid position relative to HXB2 numbering. The Y-axis represents the average amino acid divergence from the parent strain.
e,f, Glycosylation site divergence in N6-treated (e,f) mice as compared to the parental strain for $HIV_{REJO.c}$ (**e**) or HIV_{JR-CSF} (**f**) as determined by Illumina Deep Sequencing from plasma viral RNA isolated from the final experimental timepoint. The X-axis represents the envelope protein amino acid position of each potential N-linked glycosylation relative to HXB2 numbering. The Y-axis represents the average divergence from the parental

strain envelope glycosylation sites. Plots are corrected for glycan divergence observed in control mice. Potential N-linked glycosylation sites in the sequences were defined as Asn-X-Thr/Ser (NXT/S, with X being any amino acid but Pro) and the reference sequences with their respective haplotype frequencies are shown at the top of each table.

g,h, *In vitro* neutralization assay of $HIV_{REJO.c}$ (**g**) or $HIV_{JR\text{-}CSF}$ (**h**) harboring divergent amino acids identified in c and d, against serial dilutions of N6. Data are plotted as mean ± s.e.m.

i,j, *In silico* viral growth curves of $HIV_{REJO.c}$ (**i**) or $HIV_{JR\text{-}CSF}$ (**j**) harboring divergent amino acids identified in c and d, in activated PBMC's generated using growth rates derived from QuickFit assays. Data are plotted as mean ± 95% C.I.

Extended Data Fig. 5: Vectored delivery of PGDM1400 selects for multiple mutations impacting glycosylation.

a, b, Haplotypes of individual mice infected with $HIV_{REJO.c}$ (**a**) or $HIV_{JR\text{-}CSF}$ (**b**) treated with vectored PGDM1400 as revealed by deep sequencing of envelope genes from plasma viral RNA obtained at the final experimental timepoint. Each row represents the consensus sequence from a single mouse. Both control (top) and PGDM1400 (bottom) treated mice are shown. Numbers to the right of the bottom box represent the geometric mean expression of PGDM1400 (µg/mL) in each animal throughout the experiment. The X-axis represents the envelope amino acid position relative to HXB2 numbering. Yellow shading denotes position of individual loops within the HIV envelope (as indicated at the top).

c,d, Amino acid divergence from the reference strain for $HIV_{REJO.c}$ (**c**) or $HIV_{JR\text{-}CSF}$ (**d**) across all PGDM1400-treated animals as determined by Illumina Deep Sequencing of envelope from plasma viral RNA isolated from the final experimental timepoint. The X-axis represents the envelope protein amino acid position relative to HXB2 numbering. The Y-axis represents the average amino acid divergence from the parent strain.

e,f, Glycosylation site divergence in PGDM1400-treated mice as compared to the parental strain for $HIV_{REJO.c}$ (**e**) or $HIV_{JR\text{-}CSF}$ (**f**) as determined by Illumina Deep Sequencing from plasma viral RNA isolated from the final experimental timepoint. The X-axis represents the envelope protein amino acid position of each potential N-linked glycosylation relative to HXB2 numbering. The Y-axis represents the average divergence from the parental strain envelope glycosylation sites. Plots are corrected for glycan divergence observed in control mice. Potential N-linked glycosylation sites in the sequences were defined as Asn-X-Thr/Ser (NXT/S, with X being any amino acid but Pro) and the reference sequences with their respective haplotype frequencies are shown at the top of each table.

g,h, *In vitro* neutralization assay of $HIV_{REJO.c}$ (**g**) or $HIV_{JR\text{-}CSF}$ (**h**) harboring divergent amino acids identified in c and d, against serial dilutions of PGDM1400. Data are plotted as mean ± s.e.m.

i,j, *In silico* viral growth curves of $HIV_{REJO.c}$ (**i**) or $HIV_{JR\text{-}CSF}$ (**j**) harboring divergent amino acids identified in c and d, in activated PBMC's generated using growth rates derived from QuickFit assays. Data are plotted as mean ± 95% C.I.

Extended Data Fig. 6: Chimeric $HIV_{REJO.c}$ and HIV_{JR-CSF} viruses exhibit similar neutralization, growth rates, and infectivity as compared to parental strains.

a, *In vitro* neutralization assay of $HIV_{REJO.c}$ (**left**) and HIV_{JR-CSF} (**right**) harboring chimeric D and V5-loops in the presence of serial dilutions of VRC07. Data are plotted as mean ± s.e.m.

b, *In silico* viral growth curve of $HIV_{REJO.c}$ (**left**) or HIV_{JR-CSF} (**right**) harboring chimeric D and V5-loops in activated PBMC's generated using growth rates derived from QuickFit assays. Data are plotted as mean ± 95% C.I.

c, ELISA-based quantitation of gp120-binding antibodies in the serum of infected humanized mice following administration of $5x10^{11}$ genome copies (GC) of AAV-luciferase or AAV-VRC07. Black arrows denote vector administration. Data are plotted as geometric mean ± geometric SD.

d, HIV viral load in plasma following intravenous infection of $HIV_{REJO.c}$ (**left**) and HIV_{JR-CSF} (**right**) harboring chimeric D and V5-loops following AAV-VRC07 administration. Each colored line depicts an individual mouse and gray shading depicts the average viral load of control animals(n=3-4). Black arrows denote vector administration. The limit of detection was 1,000 copies per mL. Data are presented as mean ± s.e.m.

Extended Data Fig. 7: Chimeric $HIV_{REJO.c}$ and HIV_{JR-CSF} with swapped V5-loops exhibit opposite escapability metrics relative to parental strains.

a, Haplotypes of individual mice infected with $HIV_{REJO.c}$ (**left**) or HIV_{JR-CSF} (**right**) harboring a chimeric V5-loop following treatment with vectored VRC07 as revealed by deep sequencing of envelope genes from plasma viral RNA obtained at the final experimental timepoint. Each row represents the consensus sequence from a single mouse. Both control (**top**) and VRC07 (**bottom**) treated mice are shown. Numbers to the right of the bottom box represent the geometric mean expression of VRC07 (µg/mL) in each animal throughout the experiment. The X-axis represents the envelope amino acid position relative to HXB2 numbering. Yellow shading denotes position of individual loops within the HIV envelope (as indicated at the top).

b, Amino acid divergence from the parental strain for $HIV_{REJO.c}$ (**left**) or HIV_{JR-CSF} (**right**) harboring a chimeric V5-loop across all animals following AAV-luciferase treatment as determined by Illumina Deep Sequencing of envelope from plasma viral RNA isolated from the final experimental timepoint. The X-axis represents the envelope protein amino acid position relative to HXB2 numbering. The Y-axis represents the average amino acid divergence from the parent strain.

c,d, Glycosylation site divergence as compared to the parental strain for $HIV_{REJO.c}$ (**left**) or HIV_{JR-CSF} (**right**) harboring a chimeric V5-loop following AAV-luciferase (**c**) or AAV-VRC07 (**d**) treatment as determined by Illumina Deep Sequencing from plasma viral RNA isolated from the final experimental time point. The X-axis represents the envelope protein amino acid position of each potential N-linked glycosylation relative to HXB2 numbering. The Y-axis represents the average divergence from the parental strain envelope glycosylation sites. Plots in (**d**) are corrected for glycan divergence observed in control mice. Potential N-linked glycosylation sites in the sequences were defined as Asn-X-Thr/Ser (NXT/S, with X being any amino acid but Pro) and the reference sequences with their respective haplotype frequencies are shown at the top of each table.

e, *In vitro* neutralization assay of $HIV_{REJO.c}$ (**left**) or HIV_{JR-CSF} (**right**) harboring a chimeric V5-loop and divergent amino acids identified in Fig 3c against serial dilutions of VRC07. Data are plotted as mean ± s.e.m.
f, *In silico* viral growth curves of $HIV_{REJO.c}$ (**left**) or HIV_{JR-CSF} (**right**) harboring a chimeric V5-loop and divergent amino acids identified in Fig 3c in activated PBMC's generated using growth rates derived from QuickFit assays. Data are plotted as mean ± 95% C.I.

Extended Data Fig. 8: $HIV_{REJO.c}$ strains harboring emtricitabine escape mutations have similar neutralization and growth rates, but exhibit increased fitness costs during VRC07 escape.
a, Geometric mean viral load of mice prior to vectored VRC07 administration with or without ART treatment (ns=non-significant (P=0.1741) (Unpaired two-tailed Student's t test)). Error bars indicate geometric SD.
b, $HIV_{REJO.c}$ viral load in plasma following intravenous infection of non-ART-treated humanized mice after receiving AAV-VRC07 Black arrow denotes vector administration. Each colored line depicts an individual mouse and gray shading depicts the average viral load of control animals (n=8). The limit of detection was 1,000 copies per mL. Data are presented as mean ± s.e.m.
c, *In vitro* neutralization assay of $HIV_{REJO.c}$ polymerase mutants as compared to the WT polymerase in the presence of serial dilutions of VRC07. Data are plotted as mean ± s.e.m.
d, *In silico* viral growth curve of $HIV_{REJO.c}$ polymerase mutants as compared to the WT polymerase in activated PBMC's generated using growth rates derived from QuickFit assays. Data are plotted as mean ± 95% C.I.
e, *In vitro* neutralization assay of $HIV_{REJO.c}$ with M184V polymerase and the indicated envelope mutants in the presence of serial dilutions of VRC07. Data are plotted as mean ± s.e.m.
f, *In silico* viral growth curve of $HIV_{REJO.c}$ with M184V polymerase and the indicated envelope mutants in activated PBMCs generated using growth rates derived from QuickFit assays. Data are plotted as mean ± 95% C.I.

METHODS

BLT Humanized Mice. BLT humanized mice were generated by the Human Immune System Mouse Program at the Ragon Institute of MGH, MIT, and Harvard. Briefly, 6- to 8-week-old female NSG mice were transplanted with human liver and thymus tissue under the kidney capsule and injected intravenously with 100,000 CD34+ cells isolated from liver tissue by AutoMACS (Miltenyi Biotec). Mice were rested for 10 weeks after surgery to allow for recovery and engraftment. All experiments were done with approval from the Institutional Animal Care and Use Committee of the MGH and conducted in accordance with the regulations of the American Association for the Accreditation of Laboratory Animal Care.

HIV production. HIV was produced by transient transfection of 293T cells with infectious molecular clone (IMC) plasmids encoding for $HIV_{REJO.c}$ or HIV_{JR-CSF} (AIDS Reagent Program NIH Cat #11746 and #2708, respectively) or plasmids containing the indicated mutations. After 48 hours, culture supernatants were collected, filtered with a 0.45-m filter, and titered using both an HIV-1 p24 antigen capture assay (Leidos Biomedical Research) and 50% tissue culture infective dose ($TCID_{50}$) assay on TZM-bl cells. $TCID_{50}$ was calculated using the Spearman-Karber formula[70].

Humanized mouse HIV infection. Prior to HIV infection, blood samples were obtained from mice and subjected to flow cytometry to determine the baseline $CD3^+$, $CD4^+$, and $CD8^+$ T cells engraftment levels. The next day, mice were intravenously infected with

either 10ng of p24 or 300 $TCID_{50}$ of $HIV_{REJO.c}$ or HIV_{JR-CSF} diluted in PBS to a volume of 50 ⌠L.

AAV virus production and administration. AAV8 viruses encoding either luciferase, 2A10, or bNAbs were produced as previously described[4]. AAV8 IM injections were performed as previously described[4]. Briefly, aliquots of previously titered viruses were thawed on ice and diluted in PBS to achieve the predetermined dose in a 40 ⌠L volume. A single 40 ⌠L injection was administered into the gastrocnemius muscle of BLT humanized mice with a 28 G insulin syringe.

Antibody quantification by ELISA. Plasma was used to determine bNAb concentrations. For detection of gp120-binding IgG, ELISA plates were coated with 2 ⌠g/mL of $HIV_{REJO.c}$ or HIV_{JR-CSF} gp120 protein per well for 1h at room temperature. For detection of PGDM1400, ELISA plates were coated with BG505 SOSIP (provided by Vaccine Research Center) at 5 ⌠g/mL or a PGDM1400-specific idiotype (provided by Dan Barouch) at 1 ⌠g/mL for 2hr at room temperature. Plates were blocked with 1% BSA (KPL) in Tris-buffered saline (TBS) overnight at 4°C. Samples were incubated in TBS plus Tween 20 (TBST) containing 1% BSA (KPL) for 1h at room temperature before incubation with 1:2,500-1:10,000-diluted horseradish peroxidase (HRP)-conjugated goat anti-human IgG-Fc antibody (Bethyl, A80-104A) for 30 min at room temperature. Samples were detected by the TMB Microwell Peroxidase substrate system (KPL). A standard curve was generated using purified VRC07, N6, or PGDM1400 (Vaccine Research Center) as appropriate for the sample.

Viral load test by quantitative RT-PCR (qRT-PCR). Viral RNA was extracted from plasma samples using the QIAamp viral RNA mini kit (Qiagen). Each RNA sample was treated with 2 U of Turbo DNase (Invitrogen) at 37°C for 30 min followed by heat inactivation at 75°C for 15 min. 10 ⌠L of the treated RNA were used in a 20 ⌠L qRT-PCR reaction with the qScript XLT one-step RT-qPCR Tough Mix, low ROX mix (Quanta Biosciences), a TaqMan probe (5'-/56-FAM/CCCACCAAC/ZEN/AGGCGGCCTTAACTG/3IABkFQ/-3') (IDT) and primers designed targeting the Pol gene of $HIV_{REJO.c}$ (CAATGGCCCCAATTTCATCA and GAATGCCGAATTCCTGCTTGA) or HIV_{JR-CSF} (CAATGGCAGCAATTTCACCA and GAATGCCAAATTCCTGCTTGA). Samples were run in triplicate on a ViiA7 Real-Time PCR system (Applied Biosystems) or a QuantStudio 12K Flex (Applied Biosystems). The following cycling conditions were used: 50°C for 10 min, 95°C for 3 min followed by 55 cycles of 95°C for 3s and 60°C for 30s. Virus titer was determined by comparison with a standard curve generated using RNA extracted from serially diluted mixture of commercially titered viral stock and pure mouse serum. The limits of detection were 1,000 copies per mL for all viral strains. For the purpose of generating Kaplan-Meier curves, viral escape was defined as the first week after AAV administration in which viral load did not decrease at least 75% relative to the prior week and was above 10^4 copies per mL, provided that a subsequent week was also above that value. Curves were analyzed for statistical significance using the Mantel-Cox Log-rank test in Graphpad Prism.

Illumina deep sequencing and identification of HIV envelope mutants. Viral RNA extracted from blood samples at the conclusion of each study was used to synthesize cDNA using the SuperScript IV Reverse Transcriptase enzyme with a strain-specific 3' primer for $HIV_{REJO.c}$ (TTGGTACTTGTGATTGCTCCATGTCTCTCC) or $HIV_{JR\text{-}CSF}$ (CCCTATCTGTTGCTGGC- TCAGCTCGTC). cDNA was subjected to nested PCR amplification with HIV-specific envelope primers that yield a 2.5-kb fragment. The first-round primers used for amplification from $HIV_{REJO.c}$ were GCAATAGTAGCATTAGTAATAGCAGGAATAATAGCA- ATAGTTGTGTGG and CTGCTCCCACCCCCTCTG; whereas the primers used for envelope amplification from $HIV_{JR\text{-}CSF}$ were GCAATAATTGTGTGGTCCATAGTACTCAT- AGAATATAGGA and CCCTATCTGTTGCTGGCTCAGCTCGTC. First-round PCR was performed with 1 to 2.5 µL from cDNA reaction using 1x Q5 reaction buffer, 5 mM dNTPs, 0.5 ⌠M of strain specific primers and 0.02U/⌠L of Q5 Hot Start High-Fidelity DNA Polymerase (NEB) in a total reaction volume of 25 ⌠L. PCR conditions for the first round were: 98°C for 30s, followed by 30 cycles of 98°C for 10s, 70°C for 30s, 72°C for 3 min, with a final extension of 72°C for 2 min. 1⌠L of first round PCR product was then used as the template for the second round PCR with identical cycling conditions and PCR mix except for the primers. The second-round primers used for envelope amplification from $HIV_{REJO.c}$ were AAAATAGACAGGTTAATTGATAGAATAAGAGATAGA-GCAGAAGACAGTG and TCATTCTTTCCCTTACAGCAGGCCATC; whereas the primers used for envelope amplification from $HIV_{JR\text{-}CSF}$ were AAAATAGATAGGTTAATTGATAAAATAAGA- GAGAGAGCAGAAGACAG and TCATTCTTTCCCTTACAGTAGACCATCCAGGC. PCR reactions were gel extracted,

diluted to 0.15 ng/⌠L in UV-irradiated water and subjected to Nextera XT Illumina library preparation. PCR products were quantified using Qubit and D5000 ScreenTape System (Agilent). The library pool was denatured with 0.2 N NaOH, diluted to 4 nM, spiked with 10% PhiX to improve sequence diversity and quality and subjected to 2 x 250 or 2 x 300 paired-end sequencing on the Illumina MiSeq.

Envelope Escape Mutant Analysis. Sequencing reads were filtered for quality using fastp[71] and aligned to a reference sequence specific to the viral strain under analysis using Bowtie2[72]. The alignments were sorted and indexed using samtools[73]. Amino acid changes were called using a custom codon aware variant caller, written in python and available on GitHub [https://github.com/Balazs-Lab/CodonCaller]. For each sample, the total divergence at each amino acid site was determined by summing the frequency of every non-WT amino acid (relative to the IMC strain sequence, meaning that synonymous mutations are not considered divergent). The group amino acid divergence (plotted in the figures) was determined by averaging the amino acid divergence across each sample at every site. Each site was numbered using the HXB2 nomenclature[74]. The analysis pipeline was run using snakemake[75] and is available on Github at [https://github.com/Balazs-Lab/Escapability].

Diversity Analysis. Similar to the envelope escape mutation analysis, sequencing reads were filtered for quality using fastp[71] and aligned to a reference sequence specific to the viral strain under analysis using Bowtie2[72]. The alignments were sorted and indexed using samtools[73]. SNVs were called using LoFreq[76]. The diversity of each

sample was determined using the SNV data to calculate the average Shannon entropy across all sites in the viral genome, as performed in similar analyses[77,78]. The Shannon entropy at each site in the genome was calculated by taking the sum of the frequency of each SNV times the natural log of the SNV frequency (frequency * ln(frequency)), multiplied by negative one. The analysis pipeline was run using snakemake [75] and is available on Github at [https://github.com/Balazs-Lab/Escapability].

Construction of HIV mutants. Individual mutations were introduced into the parental IMC vectors expressing the molecular clone using overlapping PCR with primers incorporating the desired mutations. After amplification of the *env* or *pol* gene with the mutagenesis primers using KOD Hot Start Master mix (EMD Millipore) or Q5 Hot Start Master Mix (NEB), the PCR product was purified by gel extraction (Promega) and cloned by homologous recombination into the appropriate recipient parental backbone vector using the In-Fusion HD cloning kit (Clontech). The ligation product was transformed into DH5〈 or SURE2 competent cells, and positive clones were selected for routine analytical digestion and full plasmid sequencing to confirm successful cloning of the desired mutant.

***In vitro* neutralization assay.** To compare the sensitivity of point-mutant viruses to bNAb antibody neutralization, each mutant was produced by transient transfection of 293T cells as described above and viral supernatants were titered by $TCID_{50}$ on TZM-bl cells. Then, neutralization assays were performed by mixing 20 µL of virus with 20µL of 2.5-fold serial dilutions of each antibody and incubating this mixture at 25°C for 1 h.

After the incubation, antibody virus mixtures were added to previously plated 6,000 TZM-bl cells with 75 ⌠g per mL of DEAE dextran (Sigma) and incubated at 37°C for 48 h. Cells were then lysed using luciferin-containing buffer[79] and quantitation of luciferase signal was obtained using a PHERAstar FSX plate reader (BMG LabTech). Percentage of infection was determined by calculating the difference in luminescence between test wells (cells with virus and antibody) and cell control wells (cells only) and dividing this value by the difference between the virus control wells (cells with virus) and the cell control wells. These values were plotted against antibody concentrations and fitted into a four-parameter nonlinear regression to calculate IC_{50} using GraphPad Prism 10.0.

Determination of viral fitness. *In silico* viral growth curves were generated with growth rates derived from *in vitro* QuickFit assays as described previously [57]. Briefly, human PBMCs (AllCells) were thawed and $CD4^+$ T cells were isolated using the EasySep™ Human $CD4^+$ T Cell Isolation Kit (Stem Cell Technologies). Naive $CD4^+$ T cells were resuspended in complete RPMI (cRPMI; 10% fetal bovine serum and 1% penicillin/streptomycin) supplemented with recombinant IL-2 (R&D Systemts) at 10ng/mL and 4µg/mL of anti-CD28 antibody (Biolegend), plated in 24-well plates coated with 2µg/mL of anti-CD3 antibody (Biolegend), and incubated at 37ºC and 5% CO_2 for 4 days. Cells were then pooled and incubated for another 4 days before use. Purification and activation efficiency were evaluated by flow cytometry. Previously titered viruses were three-fold serially diluted and then added to 50 ⌠L of activated $CD4^+$($1x10^5$ cells per well) plated in a 96 round-well plate. Virus and cells were spinoculated at 1200 RPM for 1 hour at 20°C, and then incubated for 24 hours at 37ºC with 5%CO_2. Cells were

washed five times with 200⌠L of cRPMI, resuspended in 200 ⌠L of fresh cRPMI plus 10 ng/mL IL-2 and finally transferred to a 96 flat-well plate. Plates were incubated at 37°C with 5% CO_2 for 6 days. 32 ⌠L of supernatant were collected daily and fresh media was added to replace the volume. Collected supernatants were immediately RNA extracted using QuickExtract DNA Extraction Solution (Biosearch Technologies) [57]. Extracted RNA was used to determine viral loads by qRT-PCR as stated above. Viral loads were used to determine growth rates and generate *in silico* growth curves using a half-maximal equation in MonolixSuite 2023R1 (Lixoft).

***In vivo* antiretroviral selection-pressure of HIV.** To select for ART-escaping HIV mutations, individual tablets of Emtriva (emtricitabine [FTC]; Gilead) or Tenvir (tenofovir disoproxil fumarate [TDF]; Cipla LTD) were crushed into a fine powder and manufactured with TestDiet 5B1Q feed (Modified LabDiet 5058 with 0.12% amoxicillin) into powder. The final concentration of these drugs in the stock food was 2.3077% (4500 mg/kg TDF, 3000 mg/kg FTC). To achieve a comparable human dose (i.e., 200 mg FTC, 300mg TDF), the Reagan-Shaw formula (Human Equivalent Dose = Animal dose (mg/kg) x animal km/human km; Km = body weight (kg)/BSA (m^2))[80] was used to translate the dose from human to mouse with the assumption that an average mouse weighs 20 g and a human weighs 60 kg. Mice maintained their weight throughout the experiment. On average mice ate 2 g of food/day and the powdered ART-food was diluted in normal TestDiet 5B1Q food to achieve ingestion of the corresponding target human dose per day. BLT mice were infected with $HIV_{REJO.c}$ as previously stated and after 2 weeks a dose equivalent to 0.01 times the standard drug concentration was

provided (Extended Data Fig. 8A). From weeks 3 to 6 after infection, a dose of 0.1 times was administered. Finally, the equivalent of a full human dose of ART was provided through weeks 6 to 10. After this, ART treatment was interrupted. At week 8, mice were injected with AAV expressing VRC07 or luciferase as stated above. Blood samples were collected weekly to evaluate viral loads and antibody expression.

REFERENCES

1. McCoy, L. E. & Burton, D. R. Identification and specificity of broadly neutralizing antibodies against HIV. *Immunological reviews* **275**, 11–20 (2017).
2. Sajadi, M. M. *et al.* Identification of Near-Pan-neutralizing Antibodies against HIV-1 by Deconvolution of Plasma Humoral Responses. *Cell* (2018) doi:10.1016/j.cell.2018.03.061.
3. Balazs, A. B. *et al.* Vectored immunoprophylaxis protects humanized mice from mucosal HIV transmission. *Nature Medicine* **20**, 296–300 (2014).
4. Balazs, A. B. *et al.* Antibody-based protection against HIV infection by vectored immunoprophylaxis. *Nature* **481**, 81–84 (2011).
5. Deruaz, M. *et al.* Protection of Humanized Mice From Repeated Intravaginal HIV Challenge by Passive Immunization: A Model for Studying the Efficacy of Neutralizing Antibodies In Vivo. *The Journal of Infectious Diseases* **214**, 612–616 (2016).
6. Stoddart, C. A. *et al.* Efficacy of broadly neutralizing monoclonal antibody PG16 in HIV-infected humanized mice. *Virology* **462-463C**, 115–125 (2014).
7. Veselinovic, M., Neff, C. P., Mulder, L. R. & Akkina, R. Topical gel formulation of broadly neutralizing anti-HIV-1 monoclonal antibody VRC01 confers protection against HIV-1 vaginal challenge in a humanized mouse model. *Virology* **432**, 505–510 (2012).
8. Brady, J. M. & Balazs, A. B. Antibody-mediated prevention of vaginal HIV transmission is dictated by IgG subclass in humanized mice. *SCIENCE TRANSLATIONAL MEDICINE* 15 (2022).
9. Rudicell, R. S. *et al.* Enhanced potency of a broadly neutralizing HIV-1 antibody in vitro improves protection against lentiviral infection in vivo. *Journal of Virology* **88**, 12669–12682 (2014).
10. Johnson, P. R. *et al.* Vector-mediated gene transfer engenders long-lived neutralizing

activity and protection against SIV infection in monkeys. *Nature Medicine* **15**, 901–906 (2009).

11. Julg, B. *et al.* Protection against a mixed SHIV challenge by a broadly neutralizing antibody cocktail. *Science translational medicine* **9**, eaao4235 (2017).
12. Julg, B. *et al.* Broadly neutralizing antibodies targeting the HIV-1 envelope V2 apex confer protection against a clade C SHIV challenge. *Science translational medicine* **9**, eaal1321 (2017).
13. Julg, B. *et al.* Protective Efficacy of Broadly Neutralizing Antibodies with Incomplete Neutralization Activity against Simian-Human Immunodeficiency Virus in Rhesus Monkeys. *Journal of Virology* **91**, e01187-17 (2017).
14. Moldt, B. *et al.* Highly potent HIV-specific antibody neutralization in vitro translates into effective protection against mucosal SHIV challenge in vivo. *Proceedings of the National Academy of Sciences of the United States of America* **109**, 18921–18925 (2012).
15. Mayer, K. H. *et al.* Safety, pharmacokinetics, and immunological activities of multiple intravenous or subcutaneous doses of an anti-HIV monoclonal antibody, VRC01, administered to HIV-uninfected adults: Results of a phase 1 randomized trial. *PLoS medicine* **14**, e1002435 (2017).
16. Corey, L. *et al.* Two Randomized Trials of Neutralizing Antibodies to Prevent HIV-1 Acquisition. *N Engl J Med* **384**, 1003–1014 (2021).
17. Gilbert, P. B. *et al.* Neutralization titer biomarker for antibody-mediated prevention of HIV-1 acquisition. *Nat Med* (2022) doi:10.1038/s41591-022-01953-6.
18. Badamchi-Zadeh, A. *et al.* Therapeutic Efficacy of Vectored PGT121 Gene Delivery in HIV-1-

Infected Humanized Mice. *Journal of Virology* **92**, 118 (2018).

19. Barouch, D. H. *et al.* Therapeutic efficacy of potent neutralizing HIV-1-specific monoclonal antibodies in SHIV-infected rhesus monkeys. *Nature* 1–16 (2013) doi:10.1038/nature12744.
20. Borducchi, E. N. *et al.* Antibody and TLR7 agonist delay viral rebound in SHIV-infected monkeys. *Nature* **278**, 1295 (2018).
21. Halper-Stromberg, A. *et al.* Broadly Neutralizing Antibodies and Viral Inducers Decrease Rebound from HIV-1 Latent Reservoirs in Humanized Mice. *Cell* 1–11 (2014) doi:10.1016/j.cell.2014.07.043.
22. Horwitz, J. A. *et al.* HIV-1 suppression and durable control by combining single broadly neutralizing antibodies and antiretroviral drugs in humanized mice. *Proceedings of the National Academy of Sciences of the United States of America* (2013) doi:10.1073/pnas.1315295110.
23. Julg, B. *et al.* Virological Control by the CD4-Binding Site Antibody N6 in Simian-Human Immunodeficiency Virus-Infected Rhesus Monkeys. *Journal of Virology* **91**, e00498-17 (2017).
24. Klein, F. *et al.* HIV therapy by a combination of broadly neutralizing antibodies in humanized mice. *Nature* **492**, 118–122 (2012).
25. Shingai, M. *et al.* Antibody-mediated immunotherapy of macaques chronically infected with SHIV suppresses viraemia. *Nature* 1–15 (2013) doi:10.1038/nature12746.
26. Bar, K. J. *et al.* Effect of HIV Antibody VRC01 on Viral Rebound after Treatment Interruption. *The New England journal of medicine* **375**, 2037–2050 (2016).
27. Caskey, M. *et al.* Viraemia suppressed in HIV-1-infected humans by broadly neutralizing

antibody 3BNC117. *Nature* (2015) doi:10.1038/nature14411.

28. Caskey, M. *et al.* Antibody 10-1074 suppresses viremia in HIV-1-infected individuals. *Nature Medicine* **23**, 185–191 (2017).
29. Lynch, R. M. *et al.* HIV-1 fitness cost associated with escape from the VRC01 class of CD4 binding site neutralizing antibodies. *Journal of Virology* **89**, 4201–4213 (2015).
30. Mehandru, S. *et al.* Adjunctive passive immunotherapy in human immunodeficiency virus type 1-infected individuals treated with antiviral therapy during acute and early infection. *Journal of Virology* **81**, 11016–11031 (2007).
31. Mendoza, P. *et al.* Combination therapy with anti-HIV-1 antibodies maintains viral suppression. *Nature* 1–21 (2018) doi:10.1038/s41586-018-0531-2.
32. Trkola, A. *et al.* Delay of HIV-1 rebound after cessation of antiretroviral therapy through passive transfer of human neutralizing antibodies. *Nature Medicine* **11**, 615–622 (2005).
33. Bar-On, Y. *et al.* Safety and antiviral activity of combination HIV-1 broadly neutralizing antibodies in viremic individuals. *Nature Medicine* 1–13 (2018) doi:10.1038/s41591-018-0186-4.
34. deCamp, A. *et al.* Global Panel of HIV-1 Env Reference Strains for Standardized Assessments of Vaccine-Elicited Neutralizing Antibodies. *J Virol* **88**, 2489–2507 (2014).
35. Sok, D. & Burton, D. R. Recent progress in broadly neutralizing antibodies to HIV. *Nat Immunol* **19**, 1179–1188 (2018).
36. Wu, X. *et al.* Maturation and Diversity of the VRC01-Antibody Lineage over 15 Years of Chronic HIV-1 Infection. *Cell* **161**, 470–485 (2015).
37. Diskin, R. *et al.* Increasing the Potency and Breadth of an HIV Antibody by Using Structure-

Based Rational Design. *Science* (2011) doi:10.1126/science.1213782.

38. Doria-Rose, N. A. *et al.* New Member of the V1V2-Directed CAP256-VRC26 Lineage That Shows Increased Breadth and Exceptional Potency. *J Virol* **90**, 76–91 (2016).
39. Sok, D. *et al.* Recombinant HIV envelope trimer selects for quaternary-dependent antibodies targeting the trimer apex. *Proceedings of the National Academy of Sciences of the United States of America* **111**, 17624–17629 (2014).
40. Kwon, Y. D. *et al.* A matrix of structure-based designs yields improved VRC01-class antibodies for HIV-1 therapy and prevention. *mAbs* **13**, 1946918 (2021).
41. Ledgerwood, J. E. *et al.* Safety, Pharmacokinetics, and Neutralization of the Broadly Neutralizing HIV-1 Human Monoclonal Antibody VRC01 in Healthy Adults. *Clinical and experimental immunology* (2015) doi:10.1111/cei.12692.
42. Lewis, A. D., Chen, R., Montefiori, D. C., Johnson, P. R. & Clark, K. R. Generation of Neutralizing Activity against Human Immunodeficiency Virus Type 1 in Serum by Antibody Gene Transfer. *Journal of Virology* **76**, 8769–8775 (2002).
43. Fang, J. *et al.* Stable antibody expression at therapeutic levels using the 2A peptide. *Nature Biotechnology* **23**, 584–590 (2005).
44. Fuchs, S. P. *et al.* AAV-Delivered Antibody Mediates Significant Protective Effects against SIVmac239 Challenge in the Absence of Neutralizing Activity. *PLoS Pathogens* **11**, e1005090 (2015).
45. Gardner, M. R. *et al.* AAV-expressed eCD4-Ig provides durable protection from multiple SHIV challenges. *Nature* 1–16 (2015) doi:10.1038/nature14264.
46. Brady, J. M., Baltimore, D. & Balazs, A. B. Antibody gene transfer with adeno-associated

viral vectors as a method for HIV prevention. *Immunological reviews* **275**, 324–333 (2017).

47. Welles, H. C. *et al.* Vectored delivery of anti-SIV envelope targeting mAb via AAV8 protects rhesus macaques from repeated limiting dose intrarectal swarm SIVsmE660 challenge. *PLoS Pathogens* **14**, e1007395 (2018).
48. Saunders, K. O. *et al.* Broadly Neutralizing Human Immunodeficiency Virus Type 1 Antibody Gene Transfer Protects Nonhuman Primates from Mucosal Simian-Human Immunodeficiency Virus Infection. *Journal of Virology* **89**, 8334–8345 (2015).
49. Casazza, J. P. *et al.* Safety and tolerability of AAV8 delivery of a broadly neutralizing antibody in adults living with HIV: a phase 1, dose-escalation trial. *Nat Med* (2022) doi:10.1038/s41591-022-01762-x.
50. Fang, J. *et al.* An Antibody Delivery System for Regulated Expression of Therapeutic Levels of Monoclonal Antibodies In Vivo. *Molecular therapy: the journal of the American Society of Gene Therapy* **15**, 1153–1159 (2007).
51. Melkus, M. W. *et al.* Humanized mice mount specific adaptive and innate immune responses to EBV and TSST-1. *Nature Medicine* **12**, 1316–1322 (2006).
52. Baenziger, S. *et al.* Disseminated and sustained HIV infection in CD34+ cord blood cell-transplanted Rag2-/-gamma c-/- mice. *Proceedings of the National Academy of Sciences of the United States of America* **103**, 15951–15956 (2006).
53. Sun, Z. *et al.* Intrarectal transmission, systemic infection, and CD4+ T cell depletion in humanized mice infected with HIV-1. *The Journal of experimental medicine* **204**, 705–714 (2007).
54. Ochsenbauer, C. *et al.* Generation of Transmitted/Founder HIV-1 Infectious Molecular

Clones and Characterization of Their Replication Capacity in CD4 T Lymphocytes and Monocyte-Derived Macrophages. *J Virol* **86**, 2715–2728 (2012).

55. Huang, J. *et al.* Identification of a CD4-Binding-Site Antibody to HIV that Evolved Near-Pan Neutralization Breadth. *Immunity* **45**, 1108–1121 (2016).
56. Koyanagi, Y. *et al.* Dual infection of the central nervous system by AIDS viruses with distinct cellular tropisms. *Science* **236**, 819–822 (1987).
57. Galvez, N. M. S. *et al.* QuickFit: A high-throughput RT-qPCR-based assay to quantify viral growth and fitness in vitro. 2024.07.08.602587 Preprint at https://doi.org/10.1101/2024.07.08.602587 (2024).
58. Wainburg, M. A. The impact of the M184V substitution on drug resistance and viral fitness. *Expert Review of Anti-infective Therapy* **2**, 147–151 (2004).
59. Mendoza, P. *et al.* Combination therapy with anti-HIV-1 antibodies maintains viral suppression. *Nature* 1–21 (2018) doi:10.1038/s41586-018-0531-2.
60. Julg, B. *et al.* Safety and antiviral activity of triple combination broadly neutralizing monoclonal antibody therapy against HIV-1: a phase 1 clinical trial. *Nat Med* **28**, 1288–1296 (2022).
61. Pegu, A. *et al.* Potent anti-viral activity of a trispecific HIV neutralizing antibody in SHIV-infected monkeys. *Cell Reports* **38**, 110199 (2022).
62. Lynch, R. M. *et al.* Virologic effects of broadly neutralizing antibody VRC01 administration during chronic HIV-1 infection. *Science translational medicine* **7**, 319ra206-319ra206 (2015).
63. Schoofs, T. *et al.* HIV-1 therapy with monoclonal antibody 3BNC117 elicits host immune responses against HIV-1. *Science* (2016) doi:10.1126/science.aaf0972.

64. Wise, M. C. *et al.* In vivo delivery of synthetic DNA–encoded antibodies induces broad HIV-1–neutralizing activity. *Journal of Clinical Investigation* **130**, 827–837 (2020).

65. Fellinger, C. H. *et al.* eCD4-Ig limits HIV-1 escape more effectively than CD4-Ig or a broadly neutralizing antibody. *Journal of Virology* (2019) doi:10.1128/JVI.00443-19.

66. Scheid, J. F. *et al.* HIV-1 antibody 3BNC117 suppresses viral rebound in humans during treatment interruption. *Nature* (2016) doi:10.1038/nature18929.

67. Freund, N. T. *et al.* Coexistence of potent HIV-1 broadly neutralizing antibodies and antibody-sensitive viruses in a viremic controller. *Science translational medicine* **9**, eaal2144 (2017).

68. Dingens, A. S., Arenz, D., Weight, H., Overbaugh, J. & Bloom, J. D. An Antigenic Atlas of HIV-1 Escape from Broadly Neutralizing Antibodies Distinguishes Functional and Structural Epitopes. *Immunity* (2019) doi:10.1016/j.immuni.2018.12.017.

69. Haddox, H. K., Dingens, A. S., Hilton, S. K., Overbaugh, J. & Bloom, J. D. Mapping mutational effects along the evolutionary landscape of HIV envelope. *eLife* **7**, (2018).

70. Ramakrishnan, M. A. Determination of 50% endpoint titer using a simple formula. *World journal of virology* **5**, 85–86 (2016).

71. Chen, S., Zhou, Y., Chen, Y. & Gu, J. fastp: an ultra-fast all-in-one FASTQ preprocessor. *Bioinformatics (Oxford, England)* **34**, i884–i890 (2018).

72. Langmead, B. & Salzberg, S. L. Fast gapped-read alignment with Bowtie 2. *Nature Methods* **9**, 357–359 (2012).

73. Li, H. *et al.* The Sequence Alignment/Map format and SAMtools. *Bioinformatics (Oxford, England)* **25**, 2078–2079 (2009).

74. Korber, B. T., Foley, B. T., Kuiken, C. L., Pillai, S. K. & Sodroski, J. G. Numbering Positions in HIV Relative to HXB2CG. *LANL* https://www.hiv.lanl.gov/content/sequence/HIV/REVIEWS/HXB2.html (2014).

75. Köster, J. & Rahmann, S. Snakemake–a scalable bioinformatics workflow engine. *Bioinformatics (Oxford, England)* **28**, 2520–2522 (2012).

76. Wilm, A. *et al.* LoFreq: a sequence-quality aware, ultra-sensitive variant caller for uncovering cell-population heterogeneity from high-throughput sequencing datasets. *Nucleic Acids Research* **40**, 11189–11201 (2012).

77. Piantadosi, A. *et al.* Metagenomic Sequencing of HIV-1 in the Blood and Female Genital Tract Reveals Little Quasispecies Diversity during Acute Infection. *Journal of Virology* **93**, (2019).

78. McCrone, J. T. & Lauring, A. S. Measurements of Intrahost Viral Diversity Are Extremely Sensitive to Systematic Errors in Variant Calling. *Journal of Virology* **90**, 6884–6895 (2016).

79. Siebring-van Olst, E. *et al.* Affordable Luciferase Reporter Assay for Cell-Based High-Throughput Screening. *J Biomol Screen* **18**, 453–461 (2013).

80. Reagan-Shaw, S., Nihal, M. & Ahmad, N. Dose translation from animal to human studies revisited. *The FASEB journal: official publication of the Federation of American Societies for Experimental Biology* **22**, 659–661 (2008).

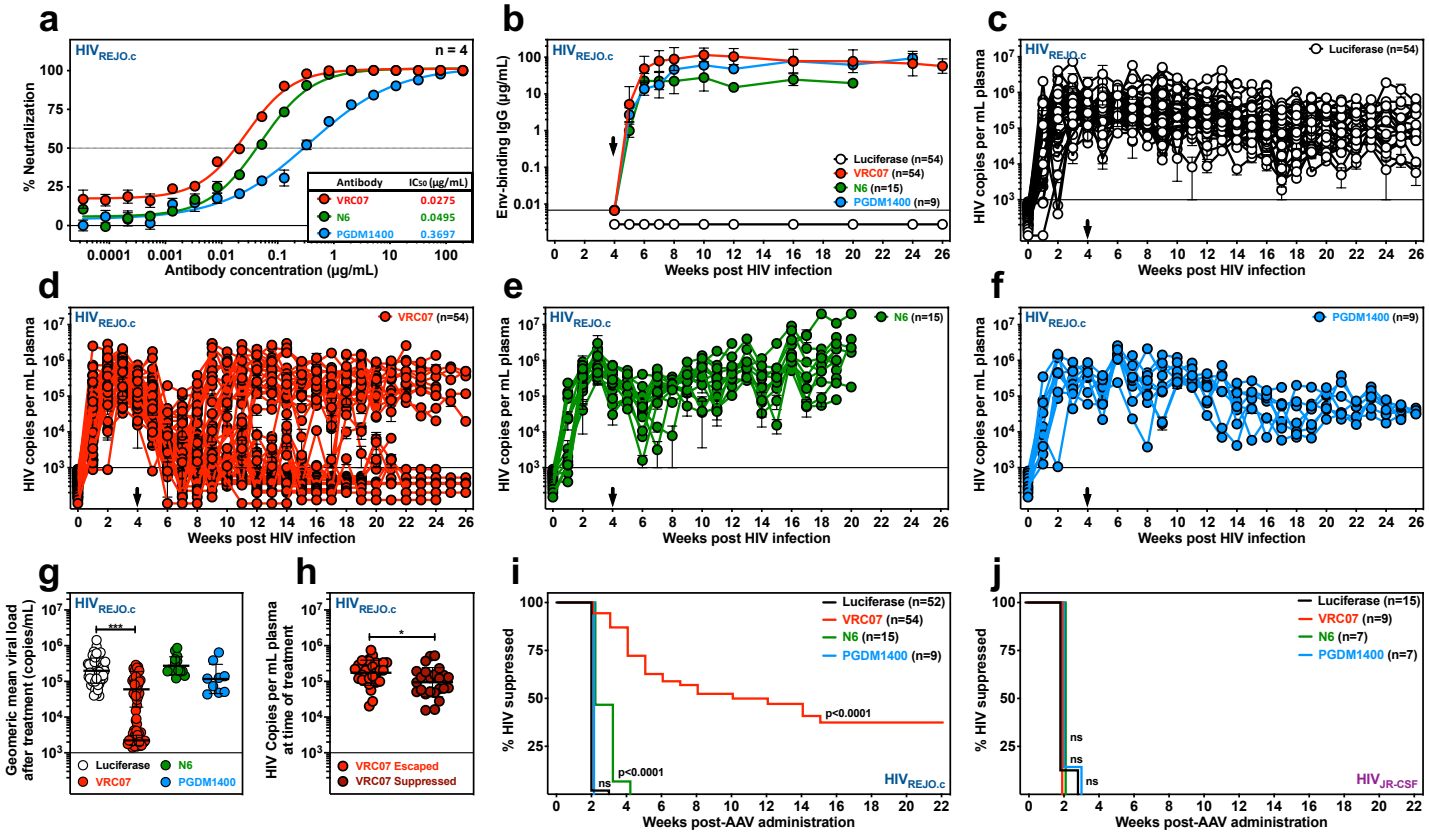

Figure 1: Vectored delivery of VRC07, but not PGDM1400 or N6, can suppress established $HIV_{REJO.c}$ infection.

a, In vitro neutralization of $HIV_{REJO.c}$ by VRC07, N6, or PGDM1400 bNAbs. Data are plotted as mean ± s.e.m.

b, ELISA-based quantitation of gp120-binding antibodies in the serum of $HIV_{REJO.c}$-infected humanized mice following administration of $5x10^{11}$ genome copies (GC) of AAV-luciferase, AAV-VRC07, AAV-N6, or AAV-PGDM1400 vectors. Black arrow denotes vector administration. Data are plotted as geometric mean ± geometric SD.

c-f, HIV viral load in plasma of $HIV_{REJO.c}$-infected mice treated with AAV-luciferase control (**c**), AAV-VRC07 (**d**), AAV-N6 (**e**), or AAV-PGDM1400 (**f**). Black arrows denote vector administration. Each colored line depicts an individual mouse. The qPCR lower limit of detection was 1,000 copies mL-1 (solid line). Data are presented as mean ± s.e.m.

g, Geometric mean viral load of mice in **c-f** following vector administration over the period of observation. (p=0.0003 (One-way ANOVA with Dunnet's post-hoc test)). Error bars indicate the geometric SD.

h, HIV viral load in plasma of $HIV_{REJO.c}$-infected mice that exhibited escape or became suppressed following AAV-VRC07 vector administration (p=0.0448 (unpaired two-tailed Student's t-test)). Data are geometric mean ± geometric SD.

i, j, Kaplan-Meier plot of viral suppression in BLT humanized mice infected with either $HIV_{REJO.c}$ (**i**) or HIV_{JR-CSF} (**j**) given the indicated bNAb-expressing vector (ns: non-significant (Mantel-Cox Log-rank test comparing against the Luciferase control)). For the purposes of clarity, % HIV suppressed is defined as the fraction of mice that had not yet escaped as described in the methods.

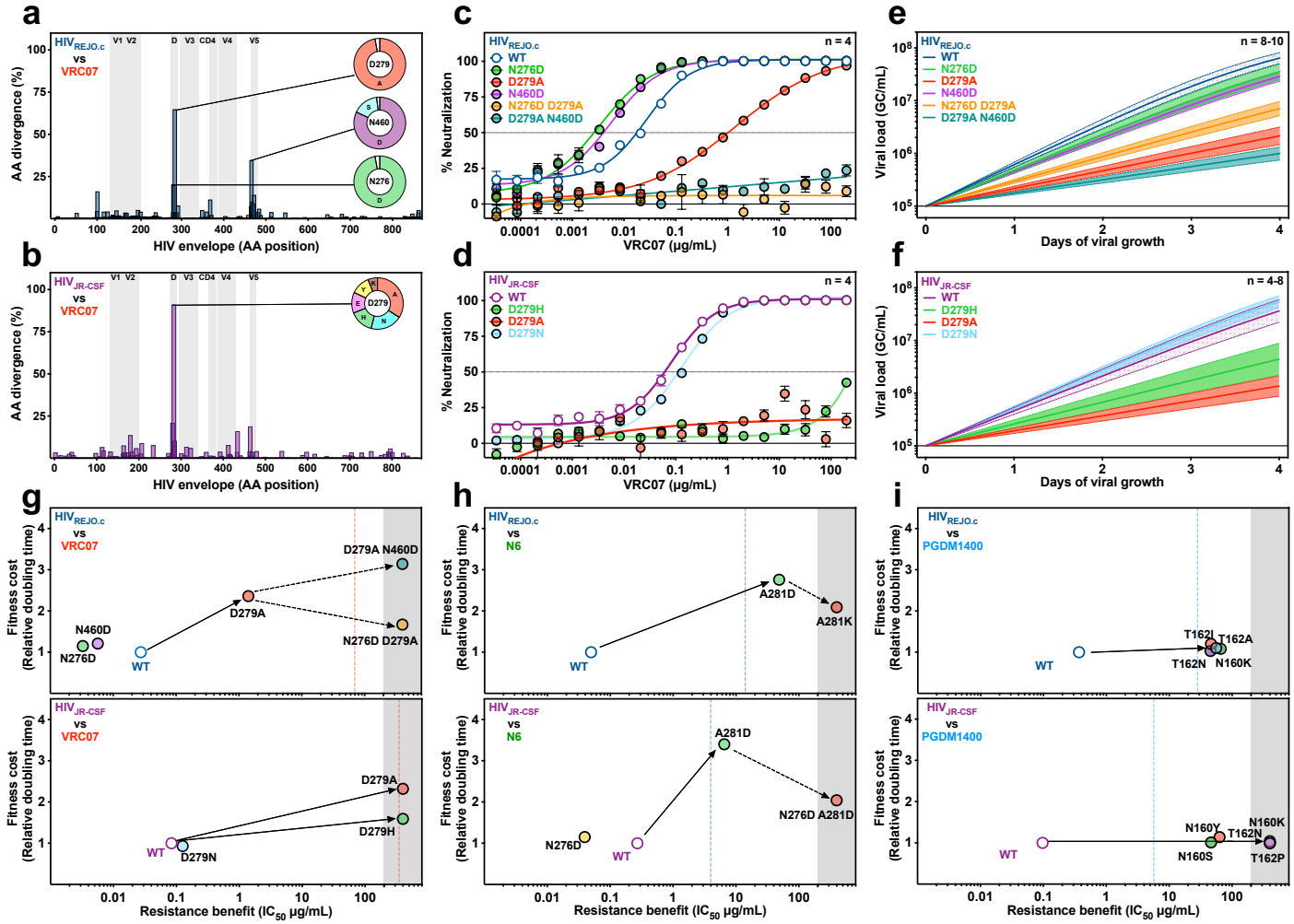

Figure 2: Escape mutations result in distinct fitness costs and resistance benefits for $HIV_{REJO.c}$ and $HIV_{JR\text{-}CSF}$.

a,b, Amino acid divergence from the reference strain for $HIV_{REJO.c}$ (**a**) or $HIV_{JR\text{-}CSF}$ (**b**) across all animals following AAV-VRC07 treatment as determined by Illumina Deep Sequencing of envelope from plasma viral RNA isolated from the final experimental timepoint. The X-axis represents the envelope protein amino acid position relative to HXB2 numbering. The Y-axis represents the average amino acid divergence from the parent strain, corrected for divergence observed in control mice.

c,d, *In vitro* neutralization assay of $HIV_{REJO.c}$ (**c**) or $HIV_{JR\text{-}CSF}$ (**d**) harboring divergent amino acids identified in **a** and **b**, against serial dilutions of VRC07. Data are plotted as mean ± s.e.m.

e,f, *In silico* viral growth curves of $HIV_{REJO.c}$ (**e**) or $HIV_{JR\text{-}CSF}$ (**f**) harboring divergent amino acids identified in a and b, in activated PBMC's generated using growth rates derived from QuickFit assays. Data are plotted as mean ± 95% C.I.

g-i, Escapability maps denoting fitness cost (relative doubling time) and resistance benefits (neutralization resistance) for each $HIV_{REJO.c}$ (**top**) or $HIV_{JR\text{-}CSF}$ (**bottom**) mutant observed during escape from VRC07 (**g**), N6 (**h**), or PGDM1400 (**i**). Dashed vertical line denotes geometric mean antibody serum concentrations after vectored bNAb administration. Shaded areas represent the limits of detection. Solid arrows represent the likely path taken with dashed arrows representing alternative paths to escape.

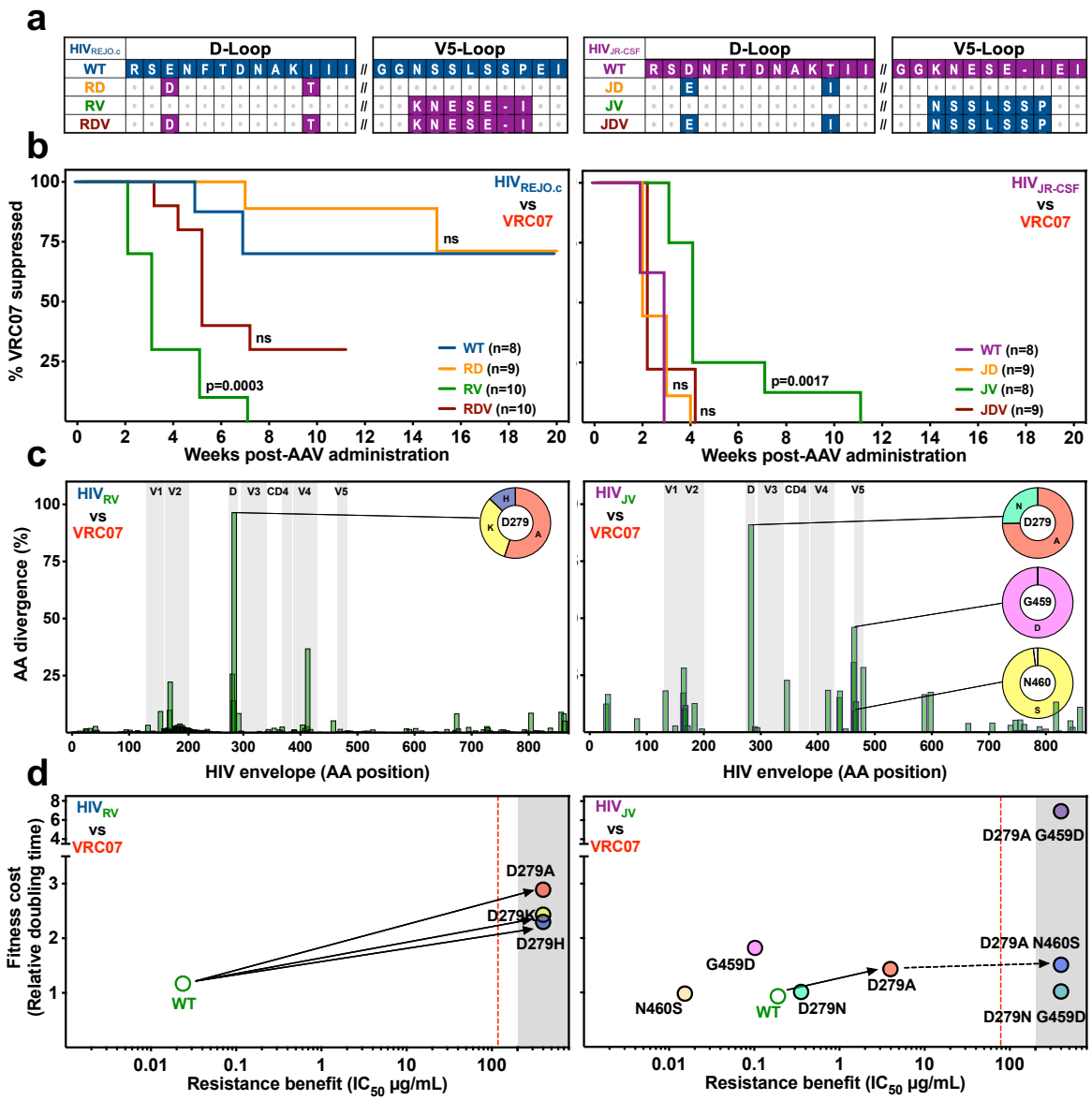

Figure 3: V5-loop sequences dictate escape outcomes for chimeric $HIV_{REJO.c}$ and HIV_{JR-CSF} viruses.
a, Diagram depicting $HIV_{REJO.c}$ and HIV_{JR-CSF} D-loop and V5-loop sequences present in each chimeric virus.
b, Kaplan-Meier plot of viral suppression in humanized mice infected with either $HIV_{REJO.c}$ (**left**) or HIV_{JR-CSF} (**right**) harboring chimeric D and V5-loops following vectored VRC07 administration (ns: non-significant (Mantel-Cox Log-rank test comparing against the WT strain)). For the purposes of clarity, % HIV suppressed is defined as the fraction of mice that had not yet escaped as described in the methods.
c, Amino acid divergence from the parental strain for $HIV_{REJO.c}$ (**a**) or HIV_{JR-CSF} (**b**) harboring a chimeric V5-loop across all animals following AAV-VRC07 treatment as determined by Illumina Deep Sequencing of envelope from plasma viral RNA isolated from the final experimental timepoint. The X-axis represents the envelope protein amino acid position relative to HXB2 numbering. The Y-axis represents the average amino acid divergence from the parent strain, corrected for divergence observed in control mice.
d, Escapability maps denoting fitness cost (relative doubling time) and resistance benefits (neutralization resistance) of mutations observed in $HIV_{REJO.c}$ (**left**) or HIV_{JR-CSF} (**right**) harboring a chimeric V5-loop during escape from VRC07. Dashed vertical line denotes geometric mean bNAb concentrations after vectored VRC07 administration. Shaded areas represent the limits of detection. Solid arrows represent the likely path taken with dashed arrows representing alternative paths to escape.

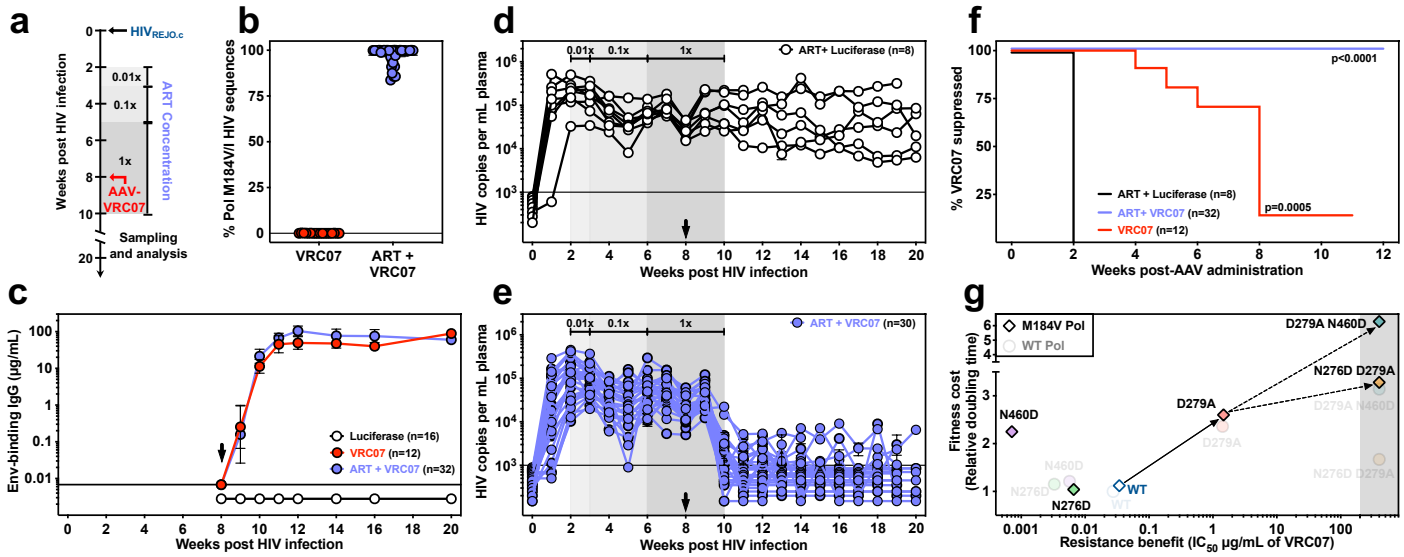

Figure 4: ART escape results in decreased viral fitness which enhances the therapeutic efficacy of vectored VRC07.

a, Diagram depicting the experimental timeline of sub-optimal ART treatment of $HIV_{REJO.c}$-infected humanized mice.

b, Percentage of M184V/I mutation observed in HIV polymerase at week 8, just prior to AAV-VRC07 administration. Data are presented as mean ± s.e.m.

c, ELISA-based quantitation of gp120-binding human IgG antibodies in serum of $HIV_{REJO.c}$-infected humanized mice following injection of $5x10^{11}$ GC of AAV-luciferase or VRC07. Black arrow denotes vector administration. Data are plotted as geometric mean ± geometric SD.

d,e, $HIV_{REJO.c}$ viral load in plasma during escape from ART drugs and following administration of (**e**) AAV-luciferase or (**f**) AAV-VRC07. Black arrows denote vector administration. Each colored line depicts an individual mouse and gray shading depicts the average luciferase viral load (n=4). The limit of detection was 1,000 copies per mL. Data are presented as mean ± s.e.m.

f, Kaplan-Meier plot of viral suppression in BLT humanized mice infected with $HIV_{REJO.c}$ treated or not with ART, given the VRC07 vector (ns: non-significant (Mantel-Cox Log-rank test comparing against the ART + Luciferase control)). For the purposes of clarity, % HIV suppressed is defined as the fraction of mice that had not yet escaped as described in the methods.

g, Escapability maps denoting fitness cost (relative doubling time) and resistance benefits (neutralization resistance) for each $HIV_{REJO.c}$ mutant observed during escape from VRC07. Shaded areas represent the limits of detection. Solid arrows represent the likely path taken with dashed arrows representing alternative paths to escape. Darker symbols (diamonds) and text represent envelope mutations on an M184V polymerase mutant background while lighter symbols (circles) and text represent the previously presented data for envelope mutations on a WT polymerase background.

Supplementary Table 1: Escape mutations yield different fitness costs and resistance benefits.

Strain	Mutations	Antibody	IC50 (ug/ml)	Growth rate
$HIV_{REJO.c}$	env WT	VRC07	0.0275	1.00
$HIV_{REJO.c}$	env WT	N6	0.0495	1.00
$HIV_{REJO.c}$	env WT	PGDM1400	0.3697	1.00
$HIV_{REJO.c}$	env N160K	PGDM1400	55.7800	1.10
$HIV_{REJO.c}$	env T162A	PGDM1400	66.0400	1.08
$HIV_{REJO.c}$	env T162I	PGDM1400	46.1400	1.20
$HIV_{REJO.c}$	env T162N	PGDM1400	45.2300	1.03
$HIV_{REJO.c}$	env N276D	VRC07	0.0033	1.15
$HIV_{REJO.c}$	env D279A	VRC07	1.4140	2.36
$HIV_{REJO.c}$	env A281D	N6	48.6100	2.76
$HIV_{REJO.c}$	env A281K	N6	>200	2.09
$HIV_{REJO.c}$	env N460D	VRC07	0.0057	1.21
$HIV_{REJO.c}$	env D279A N460D	VRC07	>200	3.14
HIV_{RD}	env WT	VRC07	0.0355	1.90
HIV_{RD}	env D279N	VRC07	0.1405	3.08
HIV_{RV}	env WT	VRC07	0.0237	1.17
HIV_{RV}	env D279A	VRC07	>200	2.89
HIV_{RV}	env D279H	VRC07	>200	2.30
HIV_{RV}	env D279K	VRC07	>200	2.43
HIV_{RDV}	env WT	VRC07	0.0332	2.14
HIV_{RDV}	env D279A	VRC07	>200	3.96
HIV_{RDV}	env D279K	VRC07	>200	4.33
$HIV_{REJO.c}$	pol M184I	VRC07	0.0226	1.08
$HIV_{REJO.c}$	pol M184V	VRC07	0.0343	1.12
$HIV_{REJO.c}$	pol M184V env D279A	VRC07	1.4650	2.60
$HIV_{REJO.c}$	pol M184V env N276D	VRC07	0.0066	1.04
$HIV_{REJO.c}$	pol M184V env N460D	VRC07	0.0007	2.25
$HIV_{REJO.c}$	pol M184V env D279A	VRC07	>200	1.67
$HIV_{REJO.c}$	pol M184V env N276D D279A	VRC07	>200	3.28
$HIV_{REJO.c}$	pol M184V env D279A N460D	VRC07	>200	6.29
HIV_{JR-CSF}	env WT	VRC07	0.0836	1.00
HIV_{JR-CSF}	env WT	N6	0.2715	1.00
HIV_{JR-CSF}	env WT	PGDM1400	0.0973	1.00
HIV_{JR-CSF}	env N160K	PGDM1400	>200	1.04
HIV_{JR-CSF}	env N160Y	PGDM1400	63.3500	1.14
HIV_{JR-CSF}	env N160S	PGDM1400	46.5200	1.01
HIV_{JR-CSF}	env T162P	PGDM1400	>200	0.99
HIV_{JR-CSF}	env T162N	PGDM1400	>200	1.00
HIV_{JR-CSF}	env N276D	N6	0.0395	1.15
HIV_{JR-CSF}	env D279A	VRC07	>200	1.59
HIV_{JR-CSF}	env D279H	VRC07	>200	2.32
HIV_{JR-CSF}	env A281D	N6	6.5360	3.40
HIV_{JR-CSF}	env N276D A281D	N6	>200	2.04
HIV_{JD}	env WT	VRC07	0.1029	1.13
HIV_{JD}	env D279A	VRC07	>200	1.94
HIV_{JD}	env D279E	VRC07	>200	1.01
HIV_{JD}	env D279H	VRC07	>200	1.06
HIV_{JD}	env D279K	VRC07	>200	1.05
HIV_{JV}	env WT	VRC07	0.1896	0.93
HIV_{JV}	env D279A	VRC07	3.9660	1.43
HIV_{JV}	env D279N	VRC07	0.3554	1.01
HIV_{JV}	env G459D	VRC07	0.1021	1.82
HIV_{JV}	env N460S	VRC07	0.0153	0.98
HIV_{JV}	env D279A G459D	VRC07	>200	6.95
HIV_{JV}	env D279A N460S	VRC07	>200	1.51
HIV_{JV}	env D279N G459D	VRC07	>200	1.02
HIV_{JDV}	env WT	VRC07	0.0520	0.92
HIV_{JDV}	env D279A	VRC07	1.3590	1.16
HIV_{JDV}	env G459D	VRC07	0.0704	5.10
HIV_{JDV}	env D279A G459D	VRC07	>200	4.14

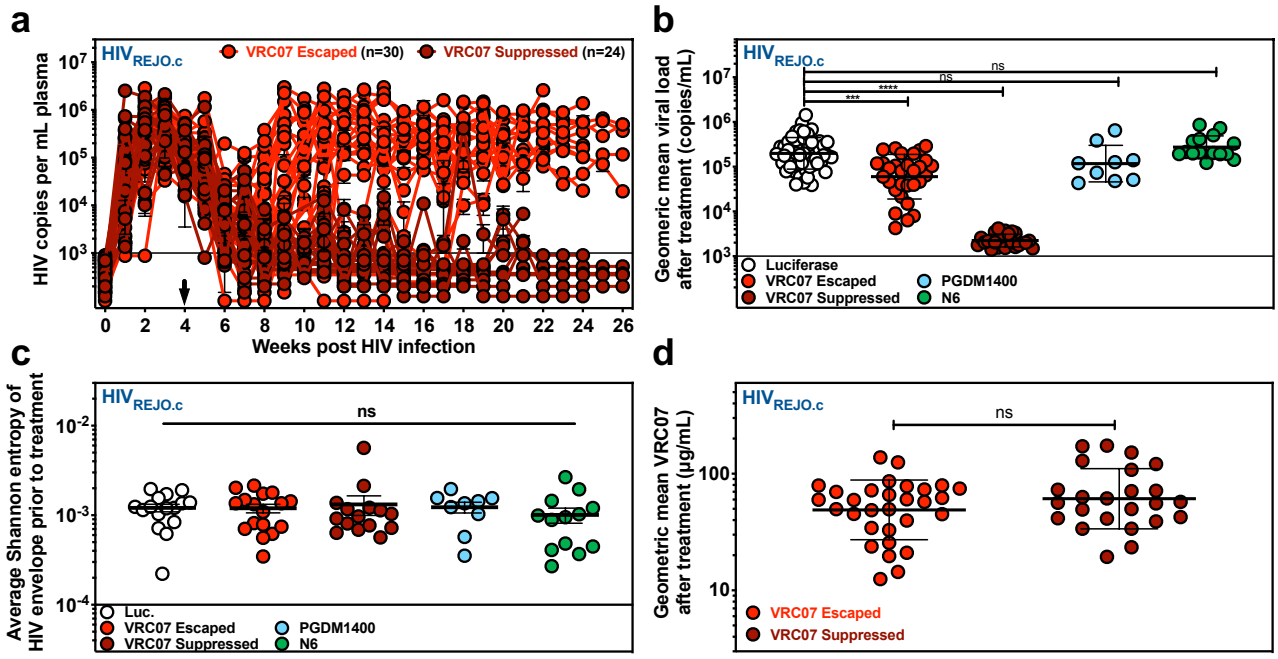

Extended Data Fig. 1: AAV-VRC07 can suppress $HIV_{REJO.c}$-infected BLT humanized mice.

a, HIV viral load in plasma of $HIV_{REJO.c}$-infected mice treated with AAV-VRC07. Each colored line depicts an individual mouse. The qPCR lower limit of detection was 1,000 copies mL^{-1} (solid line). Data are presented as mean ± s.e.m. Individual AAV-VRC07 treated mice that went on to escape or be suppressed are denoted by light or dark red colors, respectively.

b, Geometric mean viral load of mice in **a** following vector administration over the period of observation. (***:p<0.005; ****:p<0.001; ns:non-significant (One-way ANOVA with *Dunnet's* post-hoc test)). Error bars indicate geometric SD.

c, HIV diversity prior to vector administration as quantified by average Shannon entropy of envelope-amplicons measured by deep sequencing (ns=non-significant (One-way ANOVA with *Dunnet's* post-hoc test, comparing every group against the Luciferase control)). Data are presented as mean ± s.e.m.

d, Geometric mean of VRC07 antibody concentration in plasma following AAV-VRC07 vector administration in mice that exhibited escaped or suppressed $HIV_{REJO.c}$ (ns:non-significant (p=0.1305) (Unpaired two-tailed Student's t test)). Error bars indicate geometric SD.

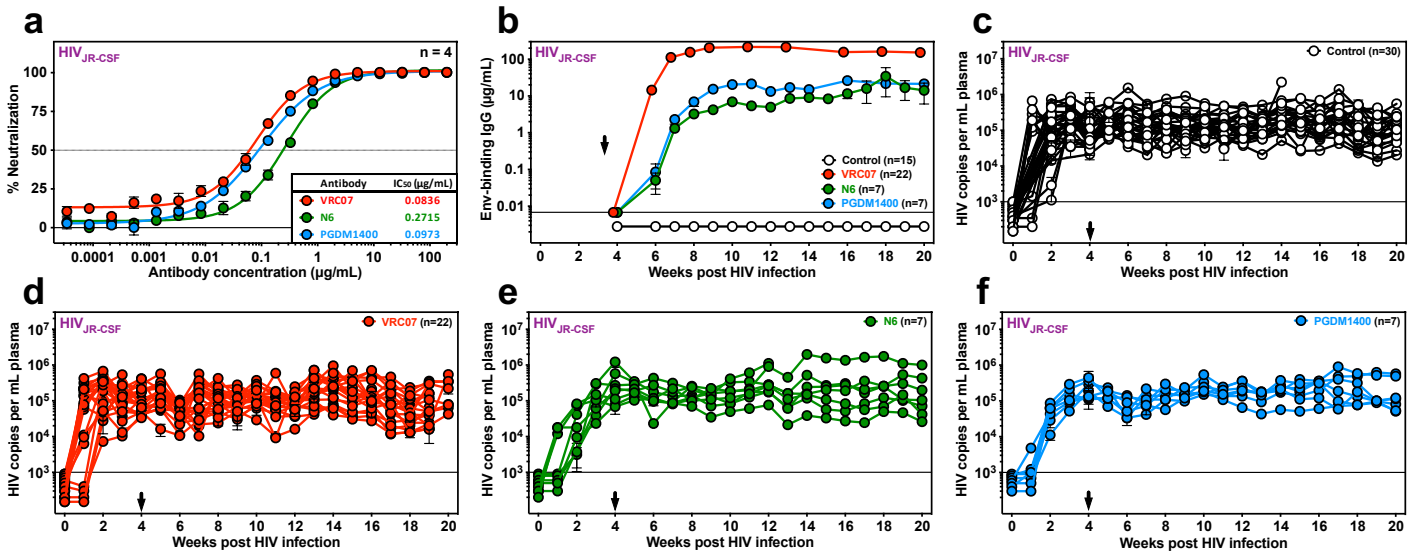

Extended Data Fig. 2: Vectored delivery of VRC07, N6, or PGDM1400 bNAbs fails to suppress HIV_{JR-CSF}-infected BLT humanized mice.

a, *In vitro* neutralization of HIV_{JR-CSF} by VRC07, PGDM1400, or N6. Data are plotted as mean ± s.e.m.

b, ELISA-based quantitation of bNAbs in serum of HIV_{JR-CSF}-infected humanized mice following injection of between 1-5x10^{11} GC of AAV-VRC07, AAV-PGDM1400, or AAV-N6. AAV-2A10 or AAV-luciferase vectors were used as negative controls. Black arrow denotes vector administration. Data are plotted as geometric mean ± geometric SD.

c-f, HIV viral load in plasma of HIV_{JR-CSF}-infected BLT mice following administration of AAV-luciferase or AAV-2A10 controls (**c**), AAV-VRC07 (**d**), AAV-N6 (**e**), or AAV-PGDM1400 (**f**). Black arrows denote vector administration. Each colored line depicts an individual mouse. The qPCR lower limit of detection was 1,000 copies mL^{-1} (solid line). Data are presented as mean ± s.e.m.

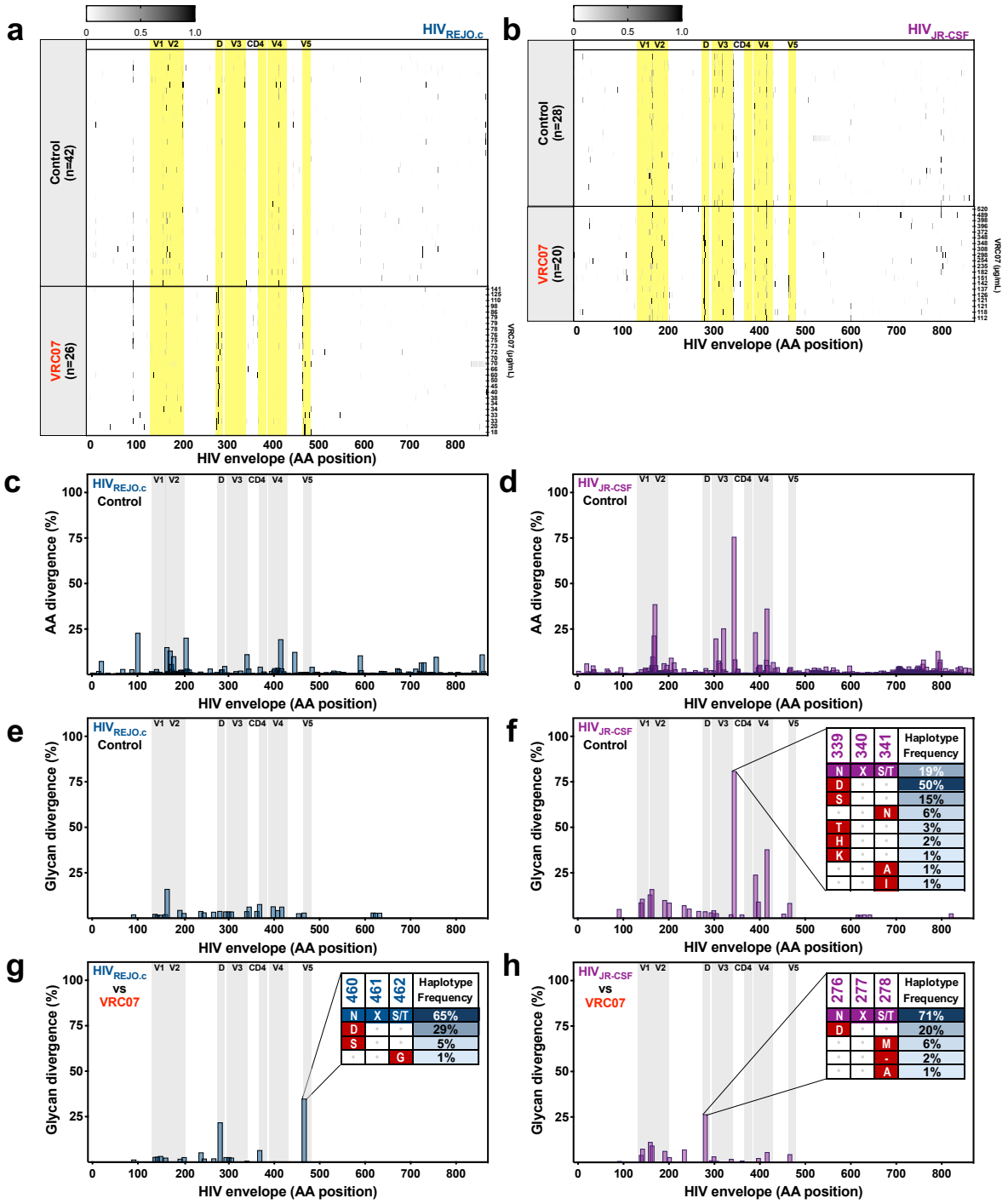

Extended Data Fig. 3: Consistent haplotypes are observed across multiple HIV-infected mice.

a,b, Haplotypes of individual mice infected with $HIV_{REJO.c}$ (**a**) or $HIV_{JR\text{-}CSF}$ (**b**) treated with vectored VRC07 as revealed by deep sequencing of envelope genes from plasma viral RNA obtained at the final experimental timepoint. Each row represents the consensus sequence from a single mouse. Both control (top) and VRC07 (bottom) treated mice are shown. Numbers to the right of the bottom box represent the geometric mean expression of VRC07 (μg/mL) in each animal throughout the experiment. The X-axis represents the envelope amino acid position relative to HXB2 numbering. Yellow shading denotes position of individual loops within the HIV envelope (as indicated at the top).

c,d, Amino acid divergence from the reference strain for $HIV_{REJO.c}$ (**c**) or $HIV_{JR\text{-}CSF}$ (**d**) across all control animals as determined by Illumina Deep Sequencing of envelope from plasma viral RNA isolated from the final experimental timepoint. The X-axis represents the envelope protein amino acid position relative to HXB2 numbering. The Y-axis represents the average amino acid divergence from the parent strain.

e-h, Glycosylation site divergence in control-treated (**e**,**f**) or VRC07-treated (**g**,**h**) mice as compared to the parental strain for $HIV_{REJO.c}$ (**e**,**g**) or $HIV_{JR\text{-}CSF}$ (**f**,**h**) as determined by Illumina Deep Sequencing from plasma viral RNA isolated from the final experimental timepoint. The X-axis represents the envelope protein amino acid position of each potential N-linked glycosylation relative to HXB2 numbering. The Y-axis represents the average divergence from the parental strain envelope glycosylation sites. Plots g and h are corrected for glycan divergence seen in control mice. Potential N-linked glycosylation sites in the sequences were defined as Asn-X-Thr/Ser (NXT/S, with X being any amino acid but Pro) and the reference sequences with their respective haplotype frequencies are shown at the top of each table.

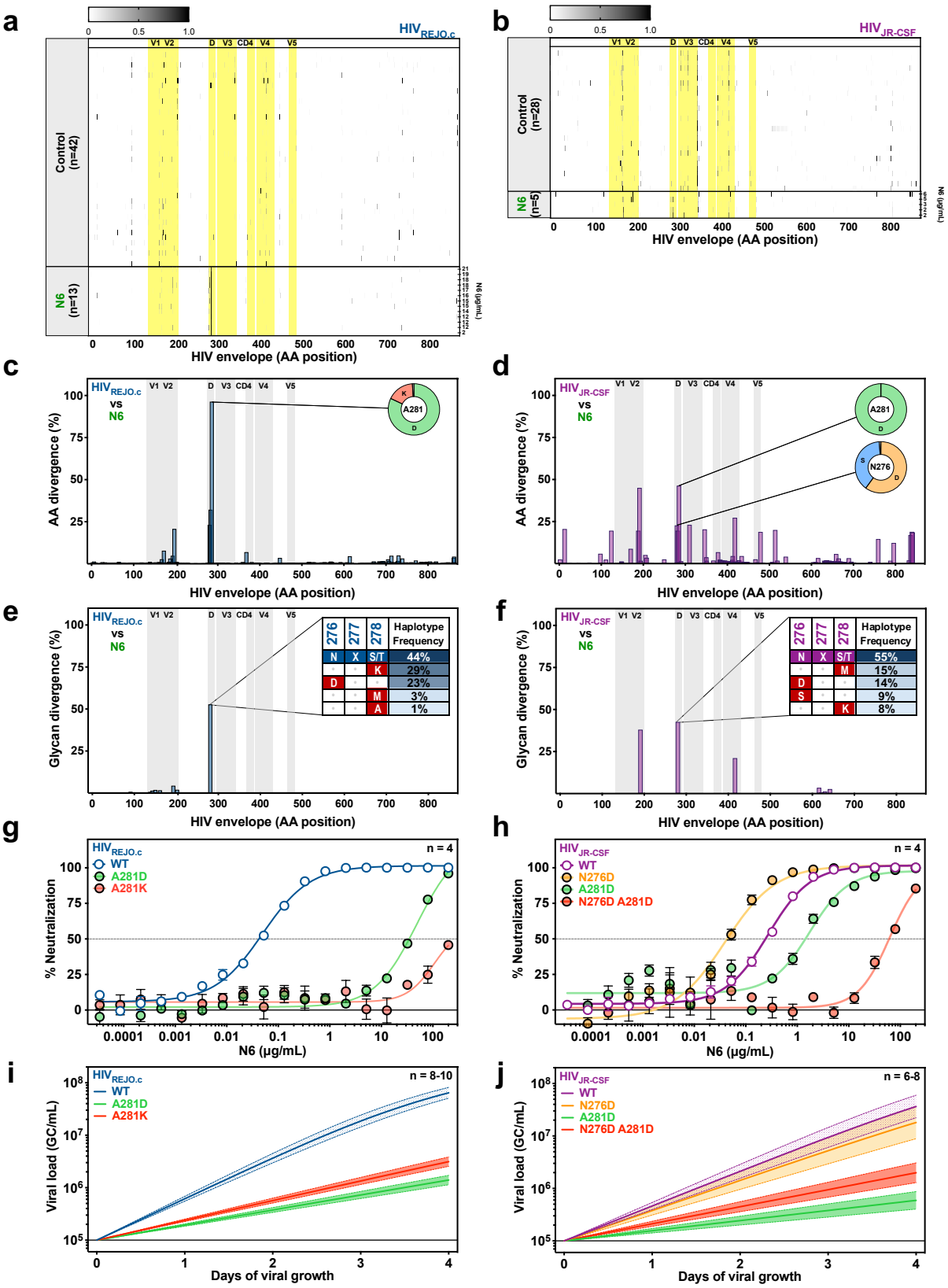

Extended Data Fig. 4: Vectored delivery of N6 selects for individual D-loop mutations that mediate resistance.

a, b, Haplotypes of individual mice infected with $HIV_{REJO.c}$ (**a**) or HIV_{JR-CSF} (**b**) treated with vectored N6 as revealed by deep sequencing of envelope genes from plasma viral RNA obtained at the final experimental timepoint. Each row represents the consensus sequence from a single mouse. Both control (**top**) and N6 (**bottom**) treated mice are shown. Numbers to the right of the bottom box represent the geometric mean expression of N6 (µg/mL) in each animal throughout the experiment. The X-axis represents the envelope amino acid position relative to HXB2 numbering. Yellow shading denotes position of individual loops within the HIV envelope (as indicated at the top).

c,d, Amino acid divergence from the reference strain for $HIV_{REJO.c}$ (**c**) or HIV_{JR-CSF} (**d**) across all N6-treated animals as determined by Illumina Deep Sequencing of envelope from plasma viral RNA isolated from the final experimental time point. The X-axis represents the envelope protein amino acid position relative to HXB2 numbering. The Y-axis represents the average amino acid divergence from the parent strain.

e,f, Glycosylation site divergence in N6-treated (e,f) mice as compared to the parental strain for $HIV_{REJO.c}$ (**e**) or HIV_{JR-CSF} (**f**) as determined by Illumina Deep Sequencing from plasma viral RNA isolated from the final experimental timepoint. The X-axis represents the envelope protein amino acid position of each potential N-linked glycosylation relative to HXB2 numbering. The Y-axis represents the average divergence from the parental strain envelope glycosylation sites. Plots are corrected for glycan divergence observed in control mice. Potential N-linked glycosylation sites in the sequences were defined as Asn-X-Thr/Ser (NXT/S, with X being any amino acid but Pro) and the reference sequences with their respective haplotype frequencies are shown at the top of each table.

g,h, *In vitro* neutralization assay of $HIV_{REJO.c}$ (**g**) or HIV_{JR-CSF} (**h**) harboring divergent amino acids identified in c and d, against serial dilutions of N6. Data are plotted as mean ± s.e.m.

i,j, *In silico* viral growth curves of $HIV_{REJO.c}$ (**i**) or HIV_{JR-CSF} (**j**) harboring divergent amino acids identified in c and d, in activated PBMC's generated using growth rates derived from QuickFit assays. Data are plotted as mean ± 95% C.I.

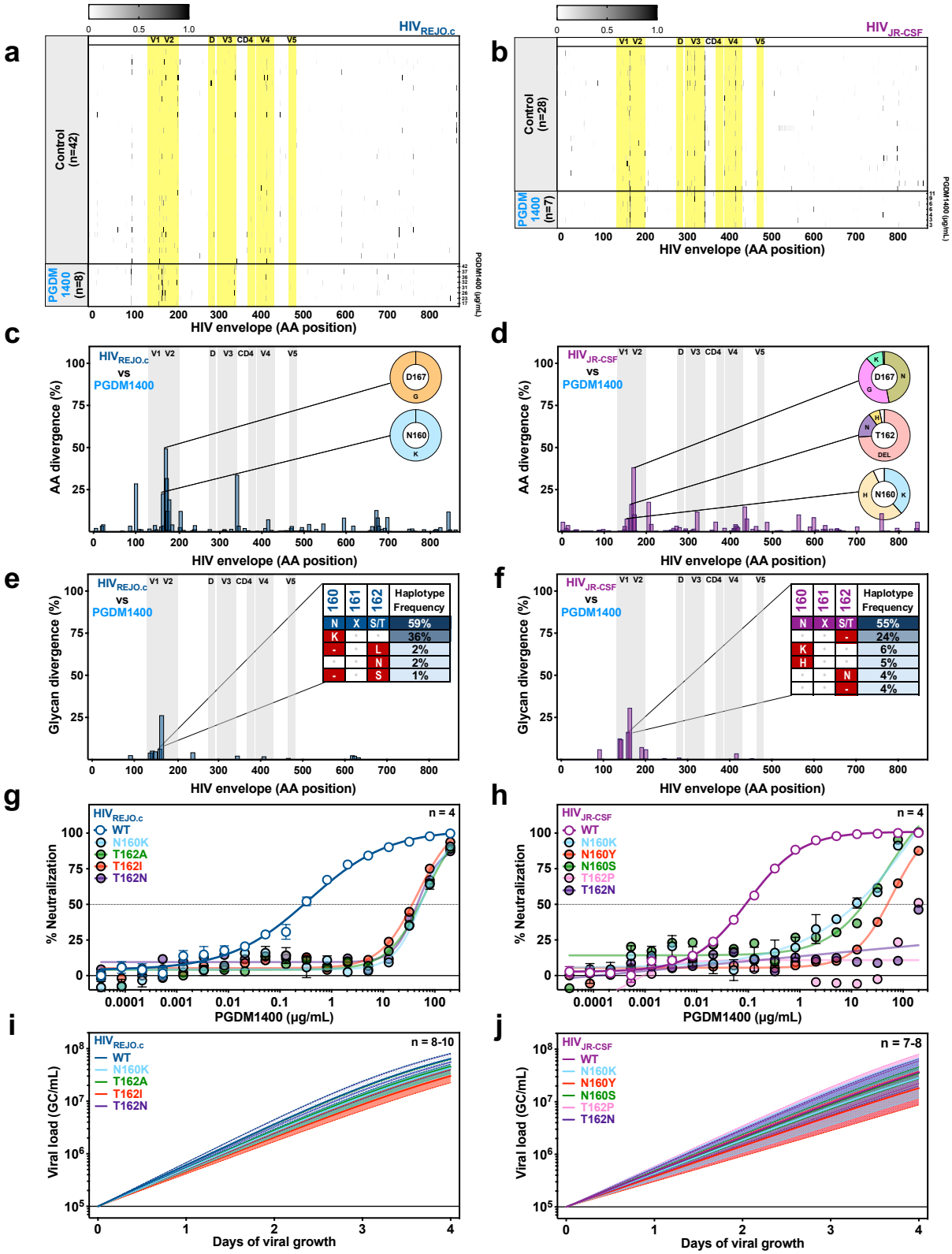

Extended Data Fig. 5: Vectored delivery of PGDM1400 selects for multiple mutations impacting glycosylation.

a, b, Haplotypes of individual mice infected with $HIV_{REJO.c}$ (**a**) or HIV_{JR-CSF} (**b**) treated with vectored PGDM1400 as revealed by deep sequencing of envelope genes from plasma viral RNA obtained at the final experimental timepoint. Each row represents the consensus sequence from a single mouse. Both control (top) and PGDM1400 (bottom) treated mice are shown. Numbers to the right of the bottom box represent the geometric mean expression of PGDM1400 (µg/mL) in each animal throughout the experiment. The X-axis represents the envelope amino acid position relative to HXB2 numbering. Yellow shading denotes position of individual loops within the HIV envelope (as indicated at the top).

c,d, Amino acid divergence from the reference strain for $HIV_{REJO.c}$ (**c**) or HIV_{JR-CSF} (**d**) across all PGDM1400-treated animals as determined by Illumina Deep Sequencing of envelope from plasma viral RNA isolated from the final experimental timepoint. The X-axis represents the envelope protein amino acid position relative to HXB2 numbering. The Y-axis represents the average amino acid divergence from the parent strain.

e,f, Glycosylation site divergence in PGDM1400-treated mice as compared to the parental strain for $HIV_{REJO.c}$ (**e**) or HIV_{JR-CSF} (**f**) as determined by Illumina Deep Sequencing from plasma viral RNA isolated from the final experimental timepoint. The X-axis represents the envelope protein amino acid position of each potential N-linked glycosylation relative to HXB2 numbering. The Y-axis represents the average divergence from the parental strain envelope glycosylation sites. Plots are corrected for glycan divergence observed in control mice. Potential N-linked glycosylation sites in the sequences were defined as Asn-X-Thr/Ser (NXT/S, with X being any amino acid but Pro) and the reference sequences with their respective haplotype frequencies are shown at the top of each table.

g,h, *In vitro* neutralization assay of $HIV_{REJO.c}$ (**g**) or HIV_{JR-CSF} (**h**) harboring divergent amino acids identified in c and d, against serial dilutions of PGDM1400. Data are plotted as mean ± s.e.m.

i,j, *In silico* viral growth curves of $HIV_{REJO.c}$ (**i**) or HIV_{JR-CSF} (**j**) harboring divergent amino acids identified in c and d, in activated PBMC's generated using growth rates derived from QuickFit assays. Data are plotted as mean ± 95% C.I.

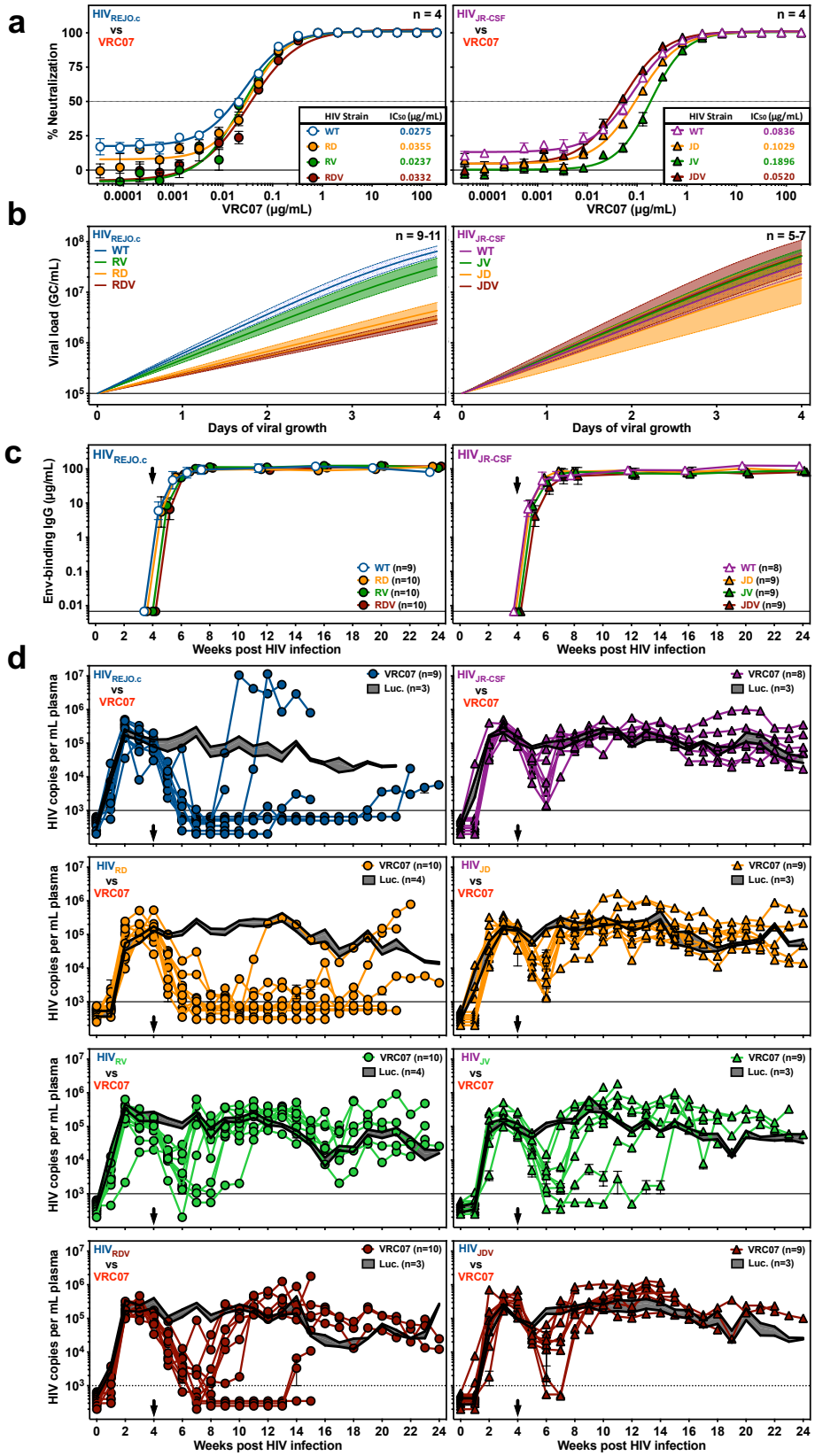

Extended Data Fig. 6: Chimeric $HIV_{REJO.c}$ and $HIV_{JR\text{-}CSF}$ viruses exhibit similar neutralization, growth rates, and infectivity as compared to parental strains.

a, *In vitro* neutralization assay of $HIV_{REJO.c}$ (**left**) and $HIV_{JR\text{-}CSF}$ (**right**) harboring chimeric D and V5-loops in the presence of serial dilutions of VRC07. Data are plotted as mean ± s.e.m.

b, *In silico* viral growth curve of $HIV_{REJO.c}$ (**left**) or $HIV_{JR\text{-}CSF}$ (**right**) harboring chimeric D and V5-loops in activated PBMC's generated using growth rates derived from QuickFit assays. Data are plotted as mean ± 95% C.I.

c, ELISA-based quantitation of gp120-binding antibodies in the serum of infected humanized mice following administration of $5x10^{11}$ genome copies (GC) of AAV-luciferase or AAV-VRC07. Black arrows denote vector administration. Data are plotted as geometric mean ± geometric SD.

d, HIV viral load in plasma following intravenous infection of $HIV_{REJO.c}$ (**left**) and $HIV_{JR\text{-}CSF}$ (**right**) harboring chimeric D and V5-loops following AAV-VRC07 administration. Each colored line depicts an individual mouse and gray shading depicts the average viral load of control animals(n=3-4). Black arrows denote vector administration. The limit of detection was 1,000 copies per mL. Data are presented as mean ± s.e.m.

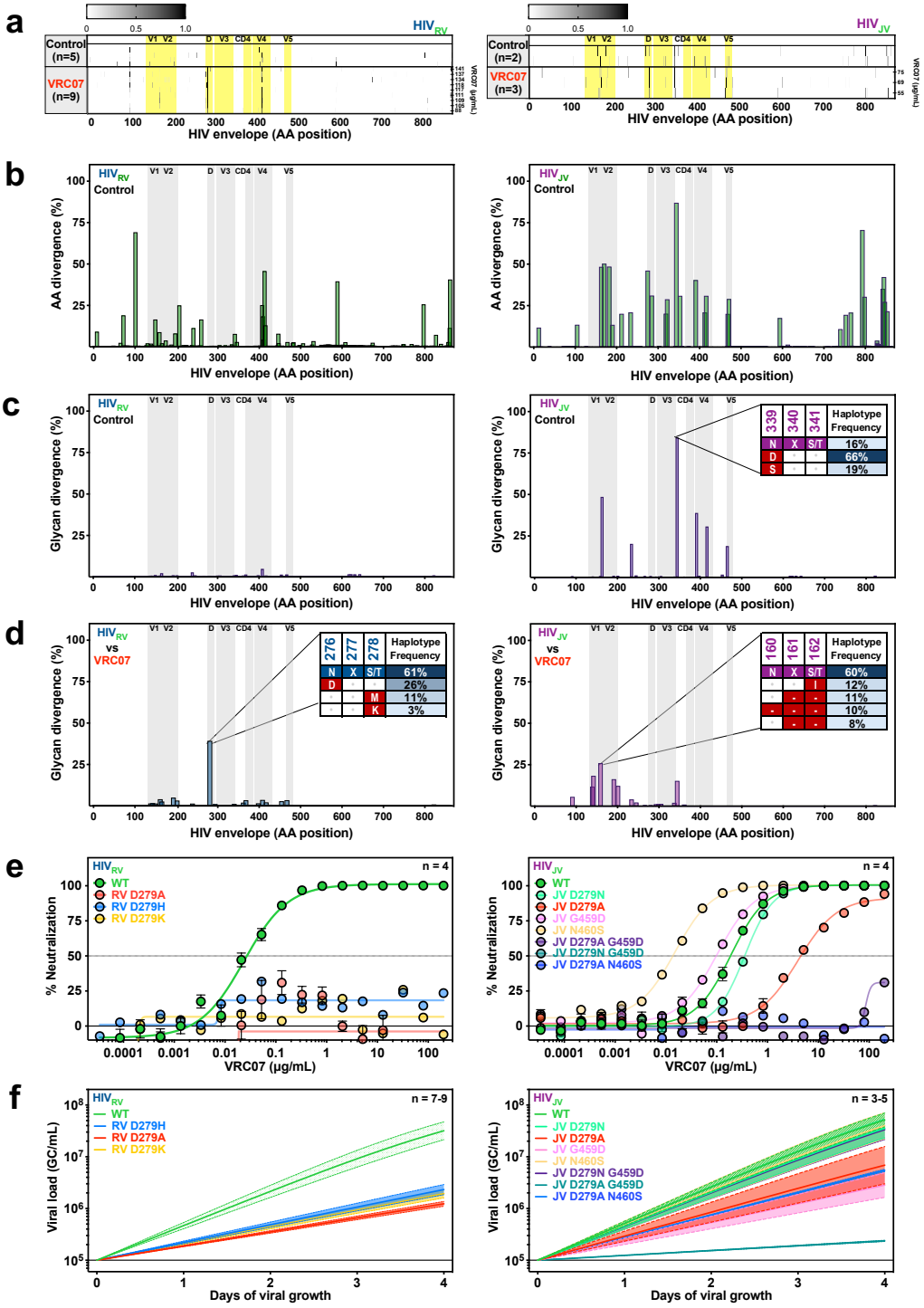

Extended Data Fig. 7: Chimeric $HIV_{REJO.c}$ and HIV_{JR-CSF} with swapped V5-loops exhibit opposite escapability metrics relative to parental strains.

a, Haplotypes of individual mice infected with $HIV_{REJO.c}$ (**left**) or HIV_{JR-CSF} (**right**) harboring a chimeric V5-loop following treatment with vectored VRC07 as revealed by deep sequencing of envelope genes from plasma viral RNA obtained at the final experimental timepoint. Each row represents the consensus sequence from a single mouse. Both control (**top**) and VRC07 (**bottom**) treated mice are shown. Numbers to the right of the bottom box represent the geometric mean expression of VRC07 (μg/mL) in each animal throughout the experiment. The X-axis represents the envelope amino acid position relative to HXB2 numbering. Yellow shading denotes position of individual loops within the HIV envelope (as indicated at the top).

b, Amino acid divergence from the parental strain for $HIV_{REJO.c}$ (**left**) or HIV_{JR-CSF} (**right**) harboring a chimeric V5-loop across all animals following AAV-luciferase treatment as determined by Illumina Deep Sequencing of envelope from plasma viral RNA isolated from the final experimental timepoint. The X-axis represents the envelope protein amino acid position relative to HXB2 numbering. The Y-axis represents the average amino acid divergence from the parent strain.

c,d, Glycosylation site divergence as compared to the parental strain for $HIV_{REJO.c}$ (**left**) or HIV_{JR-CSF} (**right**) harboring a chimeric V5-loop following AAV-luciferase (**c**) or AAV-VRC07 (**d**) treatment as determined by Illumina Deep Sequencing from plasma viral RNA isolated from the final experimental time point. The X-axis represents the envelope protein amino acid position of each potential N-linked glycosylation relative to HXB2 numbering. The Y-axis represents the average divergence from the parental strain envelope glycosylation sites. Plots in (**d**) are corrected for glycan divergence observed in control mice. Potential N-linked glycosylation sites in the sequences were defined as Asn-X-Thr/Ser (NXT/S, with X being any amino acid but Pro) and the reference sequences with their respective haplotype frequencies are shown at the top of each table.

e, *In vitro* neutralization assay of $HIV_{REJO.c}$ (**left**) or HIV_{JR-CSF} (**right**) harboring a chimeric V5-loop and divergent amino acids identified in Fig 3c against serial dilutions of VRC07. Data are plotted as mean ± s.e.m.

f, *In silico* viral growth curves of $HIV_{REJO.c}$ (**left**) or HIV_{JR-CSF} (**right**) harboring a chimeric V5-loop and divergent amino acids identified in Fig 3c in activated PBMC's generated using growth rates derived from QuickFit assays. Data are plotted as mean ± 95% C.I.

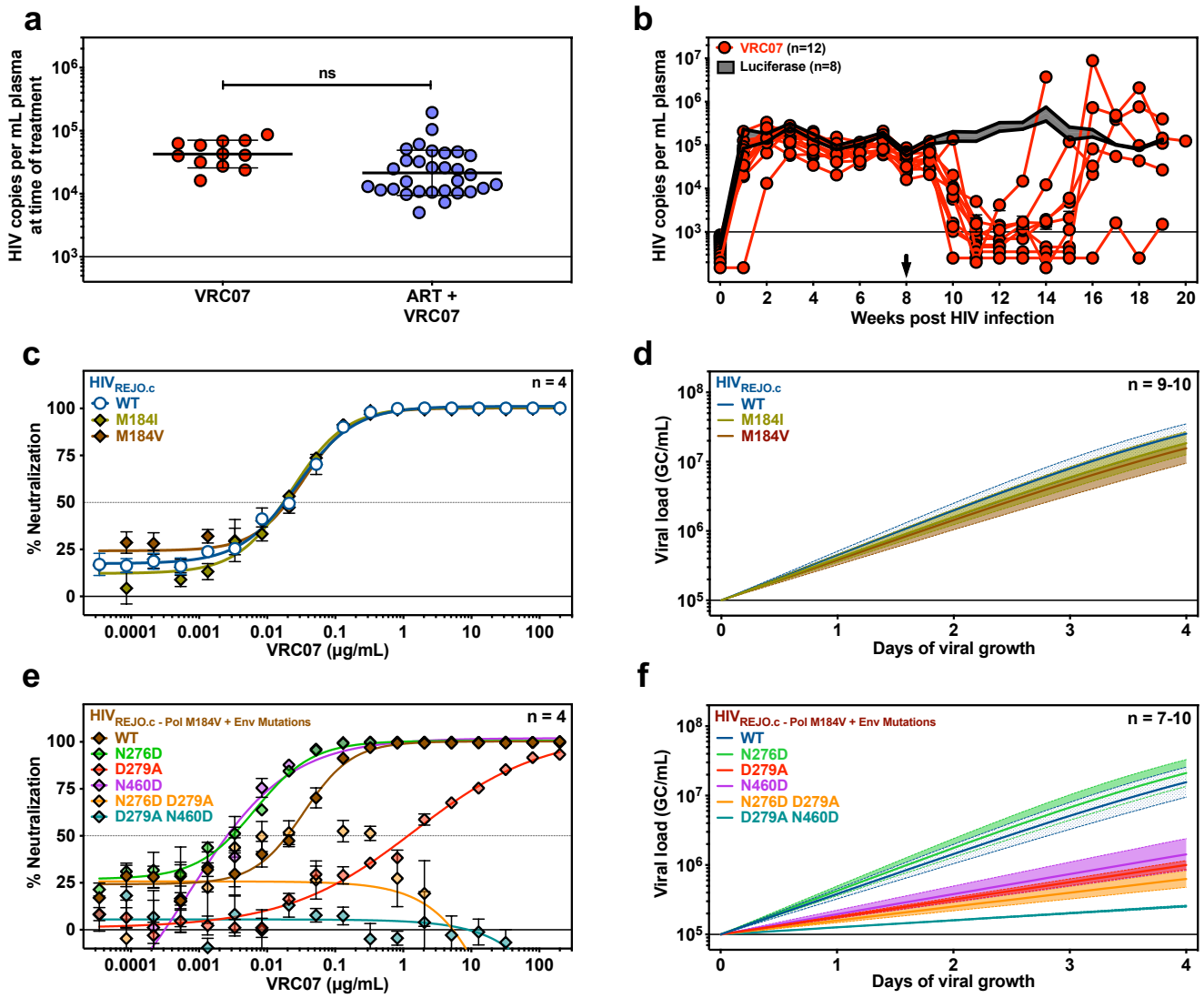

Extended Data Fig. 8: $HIV_{REJO.c}$ strains harboring emtricitabine escape mutations have similar neutralization and growth rates, but exhibit increased fitness costs during VRC07 escape.

a, Geometric mean viral load of mice prior to vectored VRC07 administration with or without ART treatment (ns=non-significant (P=0.1741) (Unpaired two-tailed Student's t test)). Error bars indicate geometric SD.

b, $HIV_{REJO.c}$ viral load in plasma following intravenous infection of non-ART-treated humanized mice after receiving AAV-VRC07 Black arrow denotes vector administration. Each colored line depicts an individual mouse and gray shading depicts the average viral load of control animals (n=8). The limit of detection was 1,000 copies per mL. Data are presented as mean ± s.e.m.

c, *In vitro* neutralization assay of $HIV_{REJO.c}$ polymerase mutants as compared to the WT polymerase in the presence of serial dilutions of VRC07. Data are plotted as mean ± s.e.m.

d, *In silico* viral growth curve of $HIV_{REJO.c}$ polymerase mutants as compared to the WT polymerase in activated PBMC's generated using growth rates derived from QuickFit assays. Data are plotted as mean ± 95% C.I.

e, *In vitro* neutralization assay of $HIV_{REJO.c}$ with M184V polymerase and the indicated envelope mutants in the presence of serial dilutions of VRC07. Data are plotted as mean ± s.e.m.

f, *In silico* viral growth curve of $HIV_{REJO.c}$ with M184V polymerase and the indicated envelope mutants in activated PBMCs generated using growth rates derived from QuickFit assays. Data are plotted as mean ± 95% C.I.

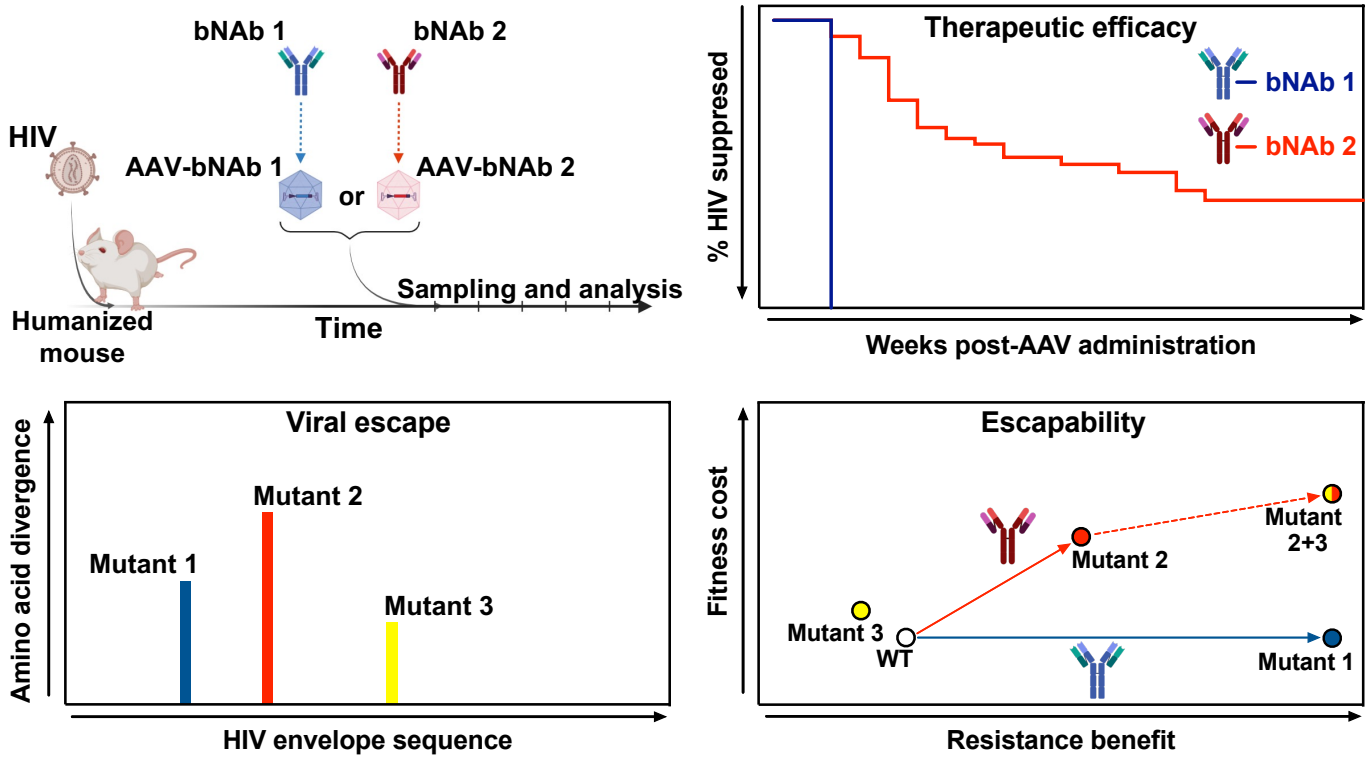

Extended Data Fig. 9: Graphical Abstract.